Check for updates

Geophysical Research Letters

RESEARCH LETTER
10.1029/2021GL094762

Key Points:

- We monitored ice motion and moulin hydraulic head along the path of a subglacial flood wave following upglacier supraglacial lake drainages
- Initial and subsequent slowdowns after the lake drainage were not caused by increased efficiency of the moulin-connected drainage system
- Our observations suggest floodwaters induced persistent basal traction increases by dewatering isolated cavities over large areas of the bed

Supporting Information:

Supporting Information may be found in the online version of this article.

Correspondence to:

J. Z. Mejia,
jzmejia@buffalo.edu

Citation:

Mejia, J. Z., Gulley, J. D., Trunz, C., Covington, M. D., Bartholomaus, T. C., Xie, S., & Dixon, T. H. (2021). Isolated cavities dominate Greenland Ice Sheet dynamic response to lake drainage. *Geophysical Research Letters*, *48*, e2021GL094762. https://doi.org/10.1029/2021GL094762

Received 14 JUN 2021
Accepted 17 SEP 2021

© 2021. American Geophysical Union. All Rights Reserved.

Isolated Cavities Dominate Greenland Ice Sheet Dynamic Response to Lake Drainage

J. Z. Mejia[1,2], J. D. Gulley[1], C. Trunz[3,4], M. D. Covington[3], T. C. Bartholomaus[5], S. Xie[6], and T. H. Dixon[1]

[1]Department of Geosciences, University of South Florida, Tampa, FL, USA, [2]Department of Geology, University at Buffalo, Buffalo, NY, USA, [3]Department of Geosciences, University of Arkansas, Fayetteville, AR, USA, [4]Department of Applied Geomatics, Université de Sherbrooke, Sherbrooke, QC, Canada, [5]Department of Earth and Spatial Sciences, University of Idaho, Moscow, ID, USA, [6]Scripps Institution of Oceanography, University of California San Diego, La Jolla, CA, USA

Abstract Seasonal variability in the Greenland Ice Sheet's (GrIS) sliding speed is regulated by the response of the subglacial drainage system to meltwater inputs. However, the importance of channelization relative to the dewatering of isolated cavities in controlling seasonal ice deceleration remains unsolved. Using ice motion, moulin hydraulic head, and glaciohydraulic tremor measurements, we show the passing of a subglacial floodwave triggered by upglacier supraglacial lake drainages slowed sliding to wintertime background speeds without increasing the hydraulic capacity of the moulin-connected drainage system. We interpret these results to reflect an increase in basal traction caused by the dewatering of isolated cavities. These results suggest the dewatering of isolated parts of the subglacial drainage system play a key role in driving seasonal slowdowns on the GrIS.

Plain Language Summary Meltwater produced on the surface of the Greenland Ice Sheet reaches the bed by flowing into crevasses or moulins, vertical holes that connect to the ice sheet's base. Early in the summer, meltwater that reaches the bed increases water pressures within the drainage system underneath the ice sheet, increasing sliding speeds. However, later in the summer, ice sliding speeds often slowdown despite continued meltwater inputs. While these slowdowns have been attributed to the growth of subglacial conduits, recent observations suggest the drainage of hydraulically isolated cavities—pockets of water formed by ice sliding over bedrock bumps—may instead be responsible. Here, we measure surface ice motion and water pressures within moulins located several kilometers away from rapidly draining supraglacial lakes. We show the passing of a floodwave underneath the ice sheet slowed sliding to wintertime speeds without enlarging subglacial channels connected to our instrumented moulin. Instead, our results indicate the drainage of isolated cavities may be responsible for slowdowns that occur during the melt season. Accordingly, our results, similar to others, suggest increased channelization of the subglacial drainage system appears unlikely to buffer GrIS ice velocity against future meltwater inputs.

1. Introduction

Predicting the Greenland Ice Sheet's (GrIS) response to future climate warming scenarios is limited by gaps in understanding of the links between ice sheet hydrology and dynamics. Using better-studied alpine glaciers as GrIS analogs, the subglacial drainage system's hydraulic capacity is considered the primary control on sliding speeds. Ice accelerates when meltwater inputs to moulins exceed the drainage system's hydraulic capacity, causing water to back up englacially. The resulting increase in the pressure head at the bed reduces basal traction to promote sliding (Bartholomaus et al., 2008; Bartholomew et al., 2012). Ice velocity decreases during the melt season have primarily been interpreted to reflect a transition from an inefficient, distributed drainage system consisting of high-pressure linked cavities and till aquifers to an efficient drainage system consisting of low-pressure conduits (Chandler et al., 2013; Colgan et al., 2012; Sole et al., 2013; Sundal et al., 2011). Conduits are thought to be able to enlarge in order to accommodate sustained meltwater influxes and drain water from the surrounding inefficient drainage system, thereby reducing subglacial water pressures and slowing sliding speeds. Under this paradigm, the GrIS ice-dynamic response to future warming should be buffered by conduit enlargement in response to increased melting.

The shallow surface slopes and thick ice characteristic of inland parts of the GrIS ablation area may limit the growth of subglacial conduits to the extent needed to drive ice deceleration (Dow et al., 2014; Meierbachtol et al., 2013). Instead, pressure decreases within hydraulically isolated or weakly connected cavities may be responsible for seasonal decreases in ice velocity previously attributed to increased drainage system efficiency (Andrews et al., 2014; Hoffman et al., 2016). The isolated drainage system consists of water-filled cavities which form on the lee-side of bedrock bumps where sliding decouples ice from the bed (Iken & Truffer, 1997; Lliboutry, 1968; Walder, 1986). Isolated cavities exist between, and are isolated from, distributed and channelized regions of the subglacial drainage system. The exact character of the isolated system is poorly understood. High pressure areas may be entirely or partially isolated (Rada & Schoof, 2018), with some areas maintaining a weak connection to the lower pressure distributed system (Hoffman et al., 2016). Distributed and channelized parts of the drainage system modulate pressures within isolated cavities indirectly through the transfer of mechanical support (Meierbachtol et al., 2016; Murray & Clarke, 1995), or through sliding-driven fluctuations in cavity volume (Bartholomaus et al., 2011; Hoffman et al., 2011; Iken & Truffer, 1997). Because pressures within isolated or weakly connected cavities are high, these small changes in cavity volume cause water pressures to fluctuate about ice overburden pressure, modifying basal traction and, where disbursed over large areas of the bed, modulating sliding speeds (Andrews et al., 2014; Hoffman et al., 2016; Iken & Truffer, 1997; Meierbachtol et al., 2016; Rada & Schoof, 2018).

Isolated cavities can connect and drain into the distributed drainage system when large influxes of water overwhelm the subglacial drainage system. Rapid basal sliding or hydraulic jacking of the ice can create transient connections between isolated cavities and nearby parts of the distributed drainage system (e.g., the "switching" behavior previously observed by Fudge et al., 2008; Gordon et al., 1998; Murray & Clarke, 1995; Rada & Schoof, 2018). If isolated cavities are at higher pressure, the water within them will drain into the distributed system until connections subsequently close off when water pressures are low (Iken & Truffer, 1997; Rada & Schoof, 2018; Stone & Clarke, 1996). Consequently, isolated cavities that maintained high average water pressures that reduced basal traction and promoted sliding before the connection would have lower water pressures and resist sliding following the leakage. If the proposed conceptual model by Andrews et al. (2014) and Hoffman et al. (2016) applies more broadly and the drainage of isolated cavities is responsible for seasonal slowdowns rather than increased channelization, it is less clear how the GrIS will respond to future warming.

Here we report how relationships between subglacial water pressure and ice sliding speeds changed when rapidly draining supraglacial lakes triggered a subglacial floodwave that passed beneath our study site on the GrIS. Using those changes, we infer that the dewatering of isolated cavities, not increased channelization, is responsible for seasonal decreases in ice velocity. Consequently, our results demonstrate that the conceptual model of isolated cavities driving slowdowns applies to supraglacial lake drainage events.

2. Study Site and Data

2.1. Study Area

In July 2018, we established a camp in the ablation area of Sermeq Avannarleq on the western GrIS (65.6°N, 49.7°W; Ice thickness 503 ± 100 m; Figure 1; Tables S1 and S2), located over 7 km downglacier from several supraglacial lakes that drained in previous years (Morriss et al., 2013; Williamson et al., 2017) (Figure 1, Tables S1 and S2). Theoretical subglacial hydraulic potential gradients, which may provide information about subglacial flow paths connecting discrete inputs to downglacier areas (Gulley et al., 2012; Morlighem et al., 2017; Schwanghart & Kuhn, 2010), indicated our camp was located along the theoretical subglacial flow path draining these lakes (Text S1). On July 10, 2018, we instrumented PIRA moulin with a pressure transducer to measure water pressure in the most active regions of the subglacial drainage system (Text S2; Andrews et al., 2014). We measured ice motion using three Global Navigation Satellite System (GNSS) stations spanning approximately 750 m in the across-flow direction from GNSS station JEME, co-located with our instrumented moulin (Texts S3 and S4). In May 2018, we installed a seismic station near PIRA moulin to measure seismic glaciohydraulic tremor, a proxy for the subglacial flux of water within the most-connected regions of the subglacial drainage system (Text S5; Bartholomaus et al., 2015), and the occurrence of icequakes associated with nearby ice fracture (Roeoesli et al., 2016). Finally, we use meteorological data

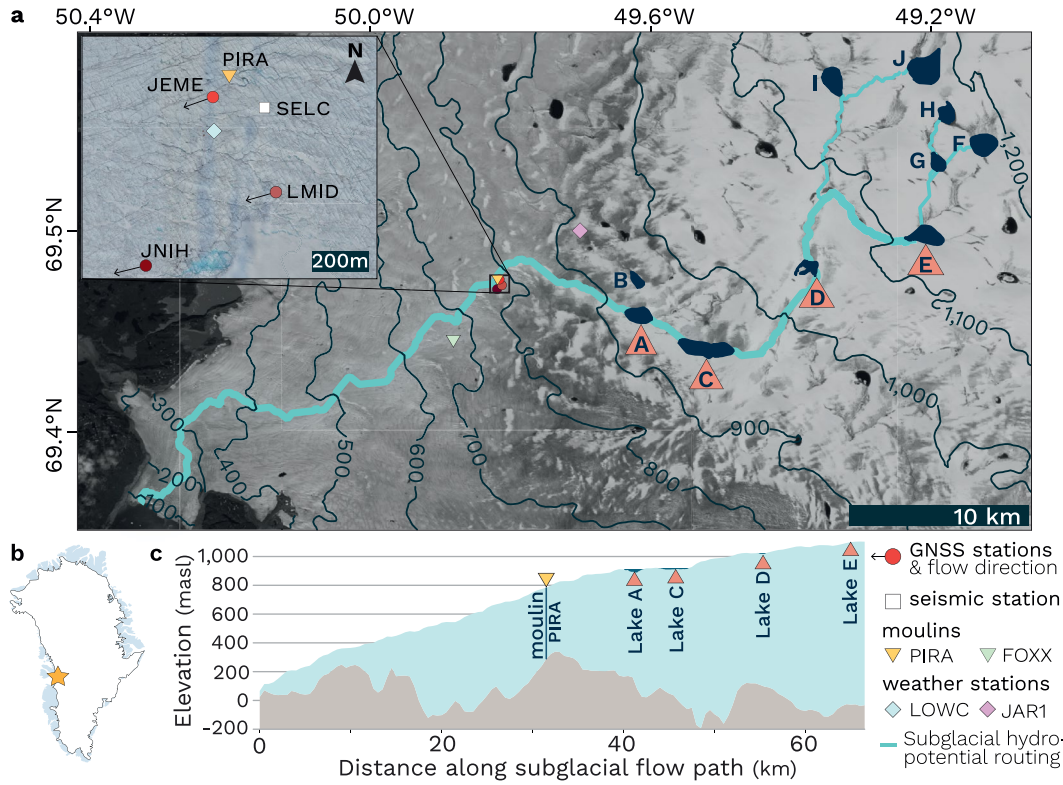


Figure 1. Study area within the ablation area of Sermeq Avannarleq, west Greenland. (a) Landsat imagery courtesy of the U.S. Geological Survey (July 21, 2018). Elevation contours from BedMachine v3. The FOXX moulin, instrumented by Andrews and others (2014), is marked for reference. Supraglacial lake maximum extents are filled in navy. The July 2018 orthophoto inset shows the PIRA moulin and instrument locations. (b) Study location in west Greenland. (c) Surface and bed elevations along the subglacial flow path extending from Lake E to the terminus (bold cyan).

from the LOWC weather station, installed at our field site, and the nearby Greenland Climate Network (GC-NET) weather station JAR1 (Steffen et al., 1996) to fill data gaps.

2.2. Moulin Instrumentation

We instrumented moulins during the 2017 (Text S6) and 2018 (PIRA moulin) melt seasons after the snow-line had retreated past the site. In both years the moulin's upper 30 m was visible and appeared vertical. We measured water pressures within each moulin using Geokon 4500HD-7.5 MPa piezometers affixed to armored cable. We instrumented moulins by lowering measured lengths of cable until the sensor reading increased with water depth, indicating we reached the water column within the moulin shaft (Text S2). We estimate an error of 20 m in our absolute moulin head measurements, arising from the uncertainty in the sensor elevation as described in detail by Andrews et al. (2014). Importantly, error in absolute moulin head does not apply to our measurements of relative change (i.e., diurnal variations) which should have an associated error on the order of centimeters (Text S2, Figure S2).

2.3. Ice Motion

We determined kinematic site positions from three on-ice GNSS stations (JEME, LMID, and JNIH) using TRACK software which uses carrier-phase differential processing relative to bedrock mounted base stations (Text S3; Herring et al., 2010; Xie et al., 2019). We used GNSS stations KAGA (28 km baseline length) and ROCK (36 km baseline) as reference stations (Figure S3). Kinematic positions were estimated using 30-s intervals that matched our receiver sampling rates. We transformed the resultant position timeseries to the along-flow and across-flow directions while preserving the vertical component of motion (Text S4; Virtanen et al., 2020). Following Hoffman et al. (2011), we calculate velocity timeseries using rolling averaging filters,

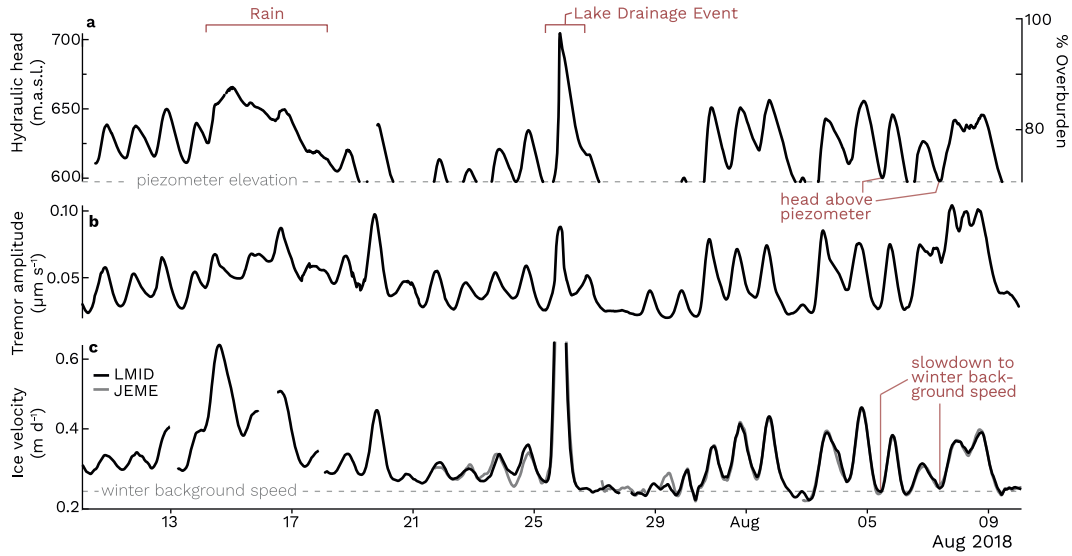


Figure 2. Moulin hydraulic head, ice velocity, and glaciohydraulic tremor, 2018 melt season (a) PIRA moulin hydraulic head. (b) Glaciohydraulic tremor amplitude. (c) Along-flow surface ice velocity. The timeseries is truncated to an upper limit of 0.6 m d^{-1} to preserve diurnal velocity minima see Figures 3 and S3 for the full range of ice velocities. A dashed line marks the winter background speed at station LMID of 0.24 m d^{-1}. The rainy period in early July is noted to explain the deviations from diurnal variability.

centered in the time domain. This methodology emphasizes variability on diurnal and event timescales while preserving extrema timing. To emphasize diurnal variability we used a 6-hr window (e.g., Figure 2c), and for the short timescales associated with the lake drainage event we used a 2-hr window (Figure 3c). To account for the remaining attenuation, we use the along-flow position timeseries, filtered with a modest 30-min window, to confirm the timing of the velocity response to the short-duration lake drainage event (Figure 3b). This 30-min filter removes spurious signals while minimizing signal attenuation.

2.4. Glaciohydraulic Tremor and Icequake Record

In April 2018, we deployed a seismic station approximately 150 m away from PIRA moulin to record local icequakes and seismic glaciohydraulic tremor amplitude, a proxy for the flux of subglacial discharge (Text S5; Bartholomaus et al., 2015). Glaciohydraulic tremor is characterized by long-duration, low-amplitude background seismic noise that varies slowly without clear onset or termination. The amplitude of these ground variations depend on the flux and pressure gradient of turbulently flowing water within efficient, well-connected conduits (Gimbert et al., 2016). The slowly varying timeseries of glaciohydraulic tremor are distinct from impulsive "icequakes" produced by ice fracture events (e.g., crevassing) that typically are found at frequencies greater than 10 Hz. Icequake characteristics during the lake drainage event are consistent with ice fracture at the glacier bed (Text S5, Figure S6).

3. Results

Before the lake drainages in late July 2018, daily meltwater production induced clear diurnal variations in moulin hydraulic head, glaciohydraulic tremor amplitude, and ice velocity (Figures 2 and S4). Moulin hydraulic head was moderately variable, with minimum values falling below the piezometer elevation of 597 m.a.s.l. (below 73 ± 12% of ice overburden pressure), and maximum values up to 666 m.a.s.l. (~88 ± 9% of overburden). Diurnal peaks in moulin water level and ice velocity were well correlated (Figure S5c), indicating PIRA moulin was well-connected to the most hydraulically efficient regions of the subglacial drainage system that control sliding on sub-diurnal timescales (Andrews et al., 2014). Further, numerical modeling work shows the volume of supraglacial discharge into our instrumented moulins can be accommodated by a single subglacial conduit (Covington et al., 2020). Importantly, before the lake drainage event, ice velocity remained above wintertime background sliding speeds at all times (Figures 2 and S4; Table S3,

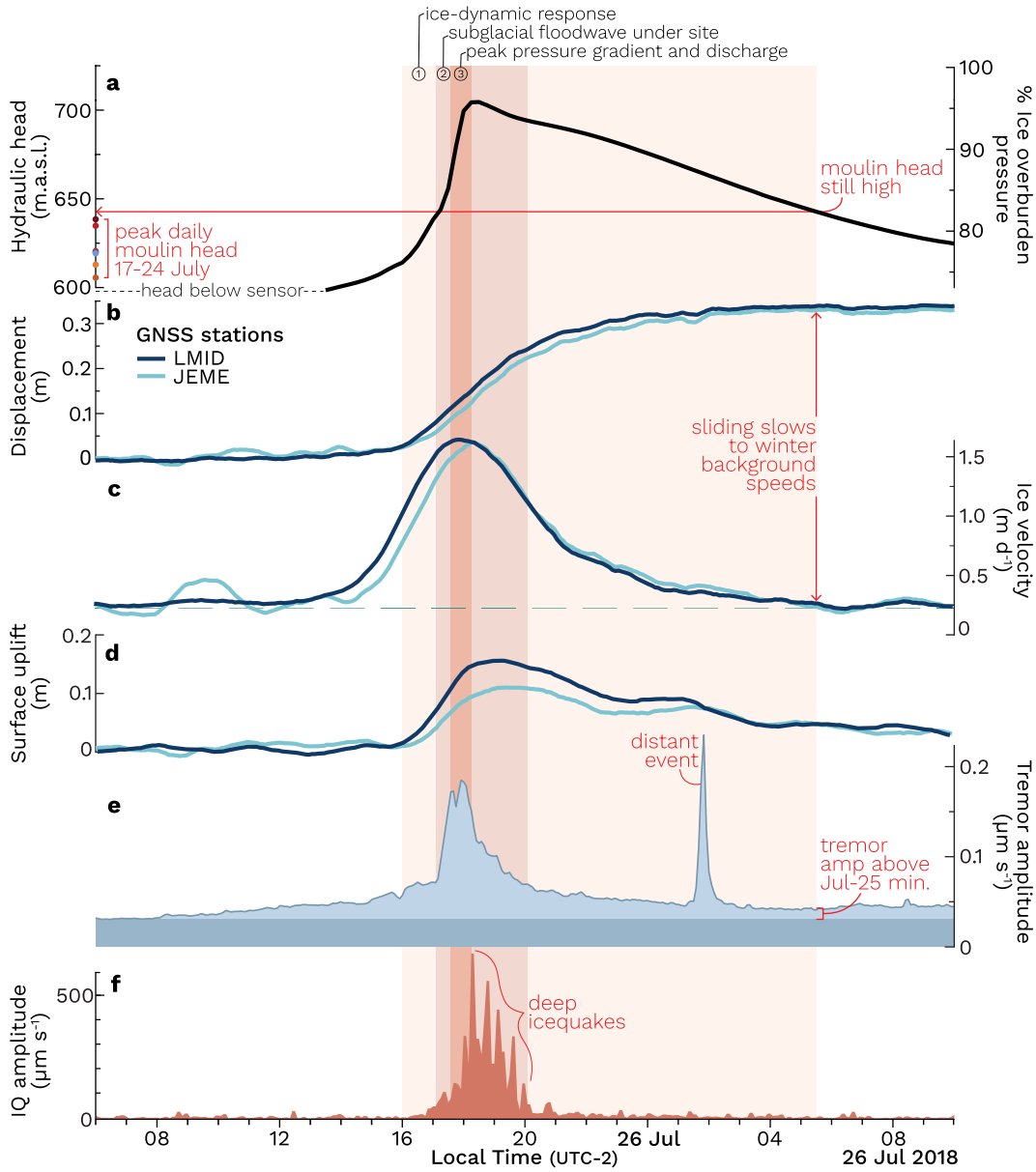


Figure 3. Coupled hydraulic, ice-dynamic, and seismic observations before, during, and following the 2018 lake drainage event. (a) PIRA hydraulic head. (b) Along-flow ice displacement and (c) ice velocity. (d) Ice surface uplift. (e) Glaciohydraulic tremor amplitude. The preceding day's diurnal minimum is shaded in darker blue. (f) Maximum icequake amplitude over 5-m intervals. Pink shading marks three phases of the lake drainage event.

Text S3), even when moulin water level dropped below the piezometer's elevation (Figures 2 and S5d; 19–23 July 2018).

Between 24 and 30 July 2018, satellite imagery captured the drainage of 10 supraglacial lakes located 8–26 km upglacier from our instrumented moulin (Figures 1 and S7; Table S2). On 25 July at 16:00 local time (UTC-02:00), moulin water level, ice sliding speeds, and uplift began increasing faster than typical diurnal fluctuations, marking the first disturbance to the connected drainage system ((1) in Figures 3a–3c). An hour after the initial pressure perturbation, glaciohydraulic tremor amplitude sharply increased between 17:15 and 18:00, suggesting the abrupt arrival of subglacial floodwaters at our site ((2) in Figure 3e). By 18:00, moulin water levels had risen 86 m, reaching 700 m.a.s.l. (~95 ± 7% of overburden). As moulin water level rose, along-flow sliding speed peaked to 1.5 m d^{-1} at stations JEME and LMID, while the ice

was uplifting most rapidly. Maximum event vertical displacement was 10 ± 5 cm and 15 ± 5 cm at JEME and LMID respectively (Figure 3d). This hydraulic and ice-dynamic response coincided with peak tremor amplitudes, indicating peak subglacial conduit pressurization and subglacial discharge past our site (e.g., Gimbert et al., 2016, (3) in Figure 3). As the subglacial floodwave began to wane and moulin water level stalled near it's peak, we observed the onset of exceptionally high amplitude, frequent icequakes at 18:15 (Figure 3f). Strong icequakes, interpreted to come from the ice sheet's bed (Text S5, Figure S6), continued as the subglacial floodwave waned. By 20:00, moulin water level and uplift were in decline, ice sliding was slowing down, icequake amplitude was getting smaller, and tremor amplitude had halved, all suggesting that most of the floodwaters had drained past our site. Over the next several hours, moulin water level gradually decreased while still remaining higher than their daily maximum levels from the previous week (Figure 3a). During this time sliding slowed, falling to winter background speeds (hereafter termed simply "background speeds") by 05:30 on 26 July, even though moulin water levels were still high. Further, similar tremor amplitudes before and after the lake drainage indicate that the channelized drainage system's hydraulic capacity had not significantly changed (Figure 3e). Altogether, these observations demonstrate that pressure decreases within the most efficient parts of the subglacial drainage system did not control ice velocity decreases. Thus, for this slowdown to occur, basal traction would need to increase over enough of the bed to counter the high water pressures in the most connected parts of the drainage system.

For the remainder of the melt season, peak diurnal moulin water level and sliding speed remained well-correlated. However, diurnal ice velocity minima recurrently fell to background speeds, without a corresponding decrease in moulin water level (Figure 2). For example, before the lake drainage on 19–25 July, moulin water level fell below the piezometer's 597 m.a.s.l. elevation while ice velocities remained above background speeds. However, after the lake drainage on 5 and 7 August, moulin water level was above the piezometer's elevation (600 and 598 m.a.s.l. respectively) yet sliding slowed to background speeds (Figure 2). This change in the relationship between diurnal minima indicates the increased basal traction triggered by the lake drainage persisted throughout the remainder of the melt season. We recorded a similar progression in 2017, but without seismic observations (Text S7).

4. Discussion

Given our observations before, during, and after lake drainages in 2017 and 2018, we infer that the slowdown to background speed was caused by increased basal traction following the drainage of water from isolated cavities that became transiently connected during the lake drainage event, and not the growth of subglacial conduits. Because moulins connect to the most efficient and well-connected parts of the subglacial drainage system (Andrews et al., 2014; Cowton et al., 2013; Gulley et al., 2012), if the subglacial floodwave increased the efficient drainage system's hydraulic capacity we should have observed lower moulin water levels whenever sliding slowed to background speeds. The absence of coincident lower moulin water levels during the initial and subsequent slowdowns indicates pressure decreases within the efficient drainage system did not control minimum ice velocities (i.e., seasonal slowdowns) in this region of the GrIS. Consequently, while pressure fluctuations within the efficient drainage system drive sliding speed increases above a given baseline, pressure decreases within unchannelized, isolated parts of the subglacial drainage system control decreases in diurnal minimum ice velocity that control the seasonal signal of ice deceleration.

4.1. Conceptual Model of Floodwave Induced Isolated Cavity Connection

We interpret the results of our study to reflect the following sequence of events. Rapid lake drainage triggered a subglacial floodwave, recorded via seismic tremor that quickly exceeded the subglacial drainage system's hydraulic capacity, as evidenced by rapid increases in moulin hydraulic head and ice motion as the floodwave approached our site. As sliding speed increased, subglacial cavities would have grown, forming new connections between linked and previously isolated or weakly connected cavities where cavities grew into each other (Figure 4a→4b). Such connections allowed high-pressures to expand across more of the bed which in turn further increased sliding speeds. Floodwaters would have continued expanding across the bed until peak discharge past our site. Once the subglacial floodwave began to recede, hydraulic damming dissipated, allowing water injected into the distributed system to drain back toward conduits (Bartholomaus et al., 2008). Water within previously isolated cavities drained through newly formed connections reducing

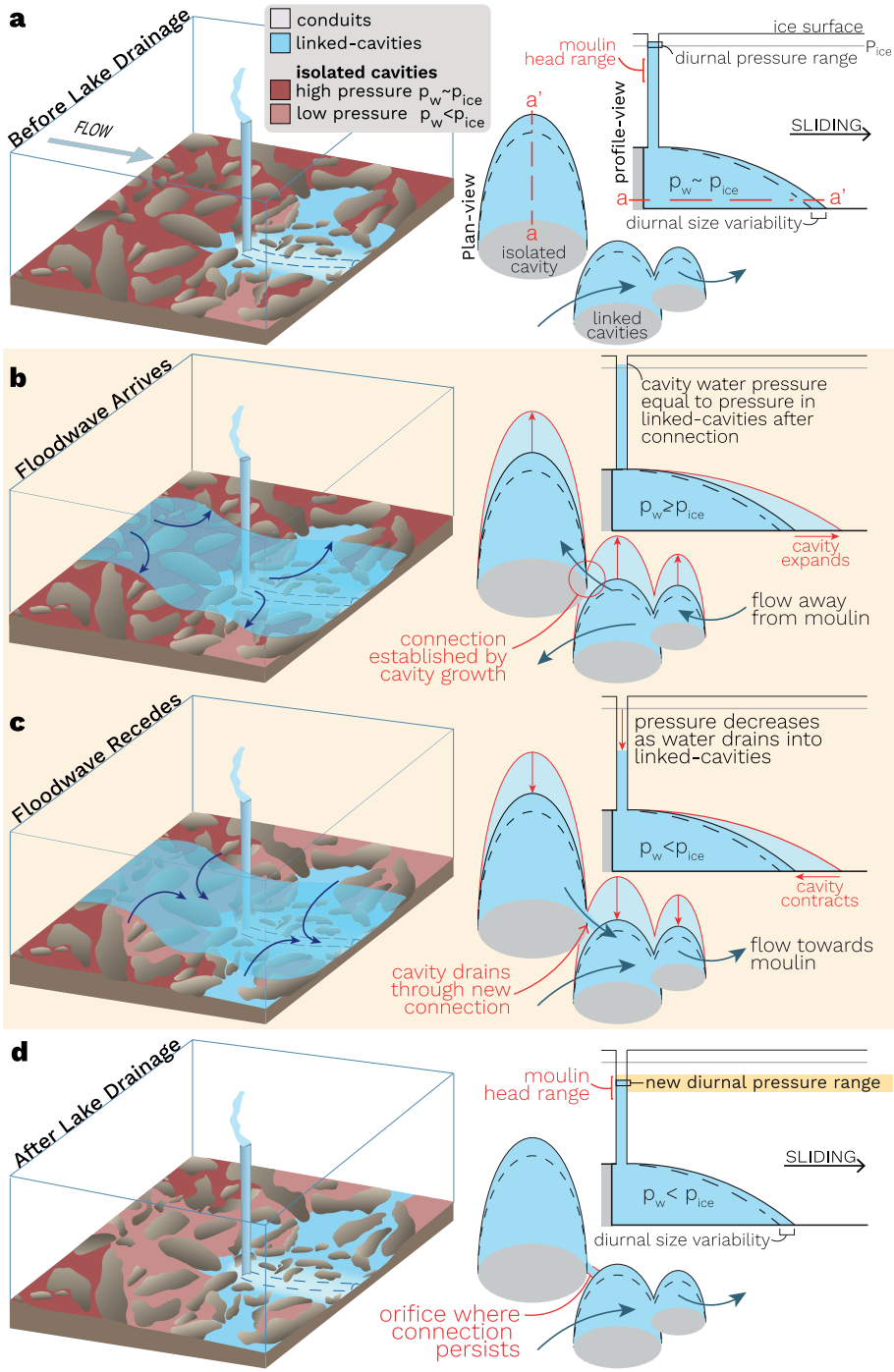


Figure 4. Conceptual model of rapid lake drainages dewatering isolated drainage system. (a) Pre-lake drainage: meltwater inputs to moulins drain through subglacial conduits (blue dashed line) which exchange water with nearby linked-cavities (blue). High-pressure isolated cavities (red). (b) Rising limb of floodwave: floodwaters overwhelm conduits, driving water laterally into the distributed system. Cavities expand and grow into each other. (c) Receding-limb of floodwave: water flows through new connections back toward conduits reducing water pressures over a large area of the bed. (d) Post-lake drainage: linked-cavities and now lower-pressure transiently connected cavities occupy a larger area of the bed.

water pressure and increasing basal traction over a large area of the bed thereby slowing sliding speeds (Figures 4c and 4d). The resulting contact pressure increase between the ice sheet and bed likely produced the high amplitude fractures at the bed that we observed as icequakes (Figure 3f). Therefore, the expansion of the distributed system at the isolated system's expense could explain the slowdown to background speeds without a pressure decrease within the moulin-connected drainage system.

Following the lake drainage event, many of the interconnections created during the event likely persisted throughout the remainder of the melt season. The hydraulic conductivity of these interconnections would vary depending on local basal conditions; ranging from values matching the distributed system to lower values characteristic of "weakly connected" cavities (i.e., Hoffman et al., 2016). For cavities with weak connections or connections that closed-off during periods of low pressure (Iken & Truffer, 1997; Murray & Clarke, 1995; Rada & Schoof, 2018), creep closure of the cavity's roof will quickly increase water pressures toward overburden (Rada & Schoof, 2018; Schoof, 2010). However, for cavities to return to their pre-lake drainage state—with pressures exceeding ice overburden (Andrews et al., 2014)—cavities would have to contract in response to a further decrease in basal sliding or fill with internally generated meltwater. Given that ice velocity does not decrease below background speeds for the melt season's duration, that the timescales required for internal meltwater generation from geothermal heat flux and frictional heating from ice sliding can be on the order of years (Hoffman et al., 2016), and that weakly connected cavities have been identified in this area of the GrIS (Andrews et al., 2014), we infer that the drainage event reduced the area of the bed occupied by high-pressure isolated cavities.

4.2. Role of Rapid Lake Drainages on GrIS Sliding

While previous studies have emphasized the role of lakes in temporarily increasing sliding speeds, our study suggests rapid lake drainages can trigger the drainage of isolated cavities following the passage of subglacial floodwaves. Consequently, the role of rapid lake drainages on ice dynamics is ambiguous. On the one hand, lake drainages increase ice velocities by triggering speedups (Selmes et al., 2011; Stevens et al., 2015) and creating stress conditions that form new moulins that deliver meltwater to the bed (Hoffman et al., 2018). On the other hand, our data show lake drainages can decrease ice velocities over large areas by dewatering isolated cavities, explaining the correlation between rapid lake drainages and the onset of seasonal ice deceleration (Andrews et al., 2018). Importantly, our observations are from an area on the ice sheet tens of kilometers away from the supraglacial lakes that drained, thereby demonstrating the ability for drainage events to alter subglacial hydrology over substantial areas of the bed.

Our work builds upon studies that identified the gradual dewatering of isolated cavities as driving seasonal GrIS ice deceleration (Andrews et al., 2014; Hoffman et al., 2016), by showing isolated cavities can also drain quickly in response to large, non-local influxes of water. Consequently, the timing and rapidity of seasonal ice deceleration may vary depending on whether areas of the ice sheet are influenced by rapid lake drainages or only local inputs to moulins. In areas not influenced by rapidly draining lakes, meltwater delivery to moulins can overwhelm the moulin-connected drainage system and drive either the incremental dewatering of isolated cavities or gradual drainage of weakly connected cavities (Andrews et al., 2014; Hoffman et al., 2016). Our results suggest that in areas influenced by rapid lake drainages (Morriss et al., 2013), massive subglacial floodwaves can expand into and connect cavities across large areas of the bed. Upon connection, the dewatering of previously isolated cavities can increase basal traction to slow sliding, irrespective of the drainage's timing within the melt season. This proposed process is consistent with observations of slowdowns following rapid lake drainage events (e.g., Andrews et al., 2018; Hoffman et al., 2011; Joughin et al., 2013; Sole et al., 2011) that cannot be explained by increased drainage system efficiency (Dow et al., 2015). Therefore, if rapid lake drainages were to occur before the moulin-connected drainage system could drain cavities, seasonal ice deceleration could occur earlier in the melt season than otherwise expected. In this way, the timing of lake drainages could aid in offsetting melt-induced acceleration.

4.3. Application to the Broader Ice Sheet

Neither rapid lake drainages nor isolated drainage systems are currently considered in the models used to predict the GrIS's sea-level rise contribution. To a large degree, their lack of inclusion stems from the

widespread use of alpine glaciers as GrIS analogs. While GrIS ice dynamics have long been interpreted in the context of better-studied alpine glaciers, there are essential differences between the two systems that may limit the applicability of alpine glacier models to the GrIS (Dow et al., 2014; Meierbachtol et al., 2013). High moulin densities, steep surface slopes, thin ice, and slow creep-closure rates of smaller alpine glaciers allow for dense networks of high-capacity channels. High channel density can lower subglacial water pressure over broad regions of the glacier bed and limit the area available for isolated cavity formation, both of which limit the impacts of isolated cavities on alpine glacier sliding.

In contrast, on the GrIS, lower moulin densities likely result in lower subglacial channel density (Banwell et al., 2016), meaning there is more bed area available for isolated cavities to form and influence ice dynamics. Inland of the margin, the GrIS's ablation area is characterized by shallow surface slopes, thick ice, and fast creep-closure rates (Dow et al., 2014, 2015; Meierbachtol et al., 2013) which may limit the ability of subglacial channels to increase their hydraulic capacity and maintain lower pressures over the timescales required to drain water from the distributed system and slow sliding. Accordingly, GrIS dynamics may be more sensitive to sustained meltwater inputs than previously thought.

5. Conclusion

Direct measurements of water pressure along a subglacial flow path showed that large influxes of meltwater from lake drainages can drain isolated cavities and slow sliding speeds without increasing the drainage system's efficiency. Building upon previous studies (Andrews et al., 2014; Hoffman et al., 2016), our results suggest that inland from the GrIS's margin, the efficient drainage system's ability to readily adjust its hydraulic capacity in response to meltwater inputs may have been overemphasized in the literature (e.g., Sole et al., 2013). Therefore, we caution against attributing ice deceleration to increased channelization without direct hydrologic measurements. When compared to the strict channelized-distributed conception of subglacial drainage, ice dynamics of the GrIS may be more sensitive to sustained meltwater inputs, even where efficient drainage does exist. Future modeling efforts should incorporate the response of unchannelized parts of the subglacial drainage system to meltwater inputs in order to achieve accurate predictions of future GrIS contributions to sea-level rise.

Conflict of Interest

The authors declare no conflicts of interest relevant to this study.

Data Availability Statement

Hydrologic (Mejia, Trunz, Covington, Gulley, & Breithaupt, 2020) and meteorologic data sets (Mejia, Trunz, Covington, & Gulley, 2020; Mejia et al., 2021) are openly available from the National Science Foundation's Arctic Data Center or via our project's portal: https://arcticdata.io/catalog/portals/moulin. Original GNSS data files are archived with UNAVCO's GAGE Facility (Fahnestock & Truffer, 2006; Mejia, Gulley, & Dixon, 2020). Basal and surface ice topography determined from Bedmachine-v3 data are available from Morlighem et al. (2017). GC-Net weather station data from JAR1 are available from Steffen et al. (1996) and are archived with Mejia et al. (2021) for convenience.

Acknowledgments
This work was supported by the United States National Science Foundation grant number 1604022. The GNSS base station and on-ice stations were provided by UNAVCO in collaboration with the National Science Foundation. Logistical support was provided by CH2MHill Polar Services. The authors thank Victoria Siegel, Charles Breithaupt, and others for their assistance in the field. We thank the Editor Mathhieu Morlighem, Florent Gimbert, and anonymous reviewers for their constructive feedback that helped to improve the manuscript.

References

Andrews, L. C., Catania, G. A., Hoffman, M. J., Gulley, J. D., Lüthi, M. P., Ryser, C., et al. (2014). Direct observations of evolving subglacial drainage beneath the Greenland Ice Sheet. *Nature*, *514*(7520), 80–83. https://doi.org/10.1038/nature13796

Andrews, L. C., Hoffman, M. J., Neumann, T. A., Catania, G. A., Lüthi, M. P., Hawley, R. L., et al. (2018). Seasonal evolution of the subglacial hydrologic system modified by supraglacial lake drainage in Western Greenland. *Journal of Geophysical Research: Earth Surface*, *123*, 1479–1496. https://doi.org/10.1029/2017JF004585

Banwell, A. F., Hewitt, I. J., Willis, I. C., & Arnold, N. S. (2016). Moulin density controls drainage development beneath the Greenland ice sheet. *Journal of Geophysical Research: Earth Surface*, *121*(12), 2248–2269. https://doi.org/10.1002/2015JF003801

Bartholomaus, T. C., Anderson, R. S., & Anderson, S. P. (2008). Response of glacier basal motion to transient water storage. *Nature Geoscience*, *1*, 33–37. https://doi.org/10.1038/ngeo.2007.52

Bartholomaus, T. C., Anderson, R. S., & Anderson, S. P. (2011). Growth and collapse of the distributed subglacial hydrologic system of Kennicott Glacier, Alaska, USA, and its effects on basal motion. *Journal of Glaciology*, *57*(206), 985–1002. https://doi.org/10.3189/002214311798843269

Bartholomaus, T. C., Larsen, C. F., Amundson, J. M., O'Neel, S., Walter, J. I., & West, M. E. (2015). Subglacial discharge at tidewater glaciers revealed by seismic tremor. *Geophysical Research Letters*, *42*, 6391–6398. https://doi.org/10.1002/2015GL064590

Bartholomew, I., Nienow, P. W., Sole, A. J., Mair, D. W., Cowton, T., & King, M. A. (2012). Short-term variability in Greenland Ice Sheet motion forced by time-varying meltwater drainage: Implications for the relationship between subglacial drainage system behavior and ice velocity. *Journal of Geophysical Research*, *117*(3), F03002. https://doi.org/10.1029/2011JF002220

Chandler, D. M., Wadham, J. L., Lis, G. P., Cowton, T., Sole, A., & Bartholomew, I., et al. (2013). Evolution of the subglacial drainage system beneath the Greenland Ice Sheet revealed by tracers. *Nature Geoscience*, *6*(3), 195–198. https://doi.org/10.1038/ngeo1737

Colgan, W., Rajaram, H., Anderson, R. S., Steffen, K., Zwally, H. J., Phillips, T., & Abdalati, W. (2012). The annual glaciohydrology cycle in the ablation zone of the Greenland ice sheet: Part 2. Observed and modeled ice flow. *Journal of Glaciology*, *58*(207), 51–64. https://doi.org/10.3189/2012JoG11J081

Covington, M. D., Gulley, J. D., Trunz, C., Mejia, J., & Gadd, W. (2020). Moulin volumes regulate subglacial water pressure on the Greenland Ice Sheet. *Geophysical Research Letters*, *47*(20), 1–9. https://doi.org/10.1029/2020GL088901

Cowton, T., Nienow, P. W., Sole, A. J., Wadham, J., Lis, G., Bartholomew, I., et al. (2013). Evolution of drainage system morphology at a land-terminating Greenlandic outlet glacier. *Journal of Geophysical Research: Earth Surface*, *118*(1), 29–41. https://doi.org/10.1029/2012JF002540

Dow, C. F., Kulessa, B., Rutt, I. C., Doyle, S. H., & Hubbard, A. (2014). Upper bounds on subglacial channel development for interior regions of the Greenland ice sheet. *Journal of Glaciology*, *60*(224), 1044–1052. https://doi.org/10.3189/2014JoG14J093

Dow, C. F., Kulessa, B., Rutt, I. C., Tsai, V. C., Pimentel, S., Doyle, S. H., et al. (2015). Modeling of subglacial hydrological development following rapid supraglacial lake drainage. *Journal of Geophysical Research: Earth Surface*, *120*, 1127–1147. https://doi.org/10.1002/2014JF003333

Fahnestock, M. A., & Truffer, M. (2006). *Greenland GNSS network—KAGA-Kangia North P.S*. UNAVCO. https://doi.org/10.7283/FQGY-4535

Fudge, T. J., Humphrey, N. F., Harper, J. T., & Tad Pfeffer, W. (2008). Diurnal fluctuations in borehole water levels: Configuration of the drainage system beneath Bench Glacier, Alaska, USA. *Journal of Glaciology*, *54*(185), 297–306. https://doi.org/10.3189/002214308784886072

Gimbert, F., Tsai, V. C., Bartholomaus, T. C., Amundson, J. M., & Walter, J. I. (2016). Subseasonal changes observed in subglacial channel pressure, size, and sediment transport. *Geophysical Research Letters*, *43*, 3786–3794. https://doi.org/10.1002/2016GL068337

Gordon, S., Sharp, M. J., Hubbard, B., Smart, C., Ketterling, B., & Willis, I. C. (1998). Seasonal reorganization of subglacial drainage inferred from measurements in boreholes. *Hydrological Processes*, *12*(1), 105–133. https://onlinelibrary.wiley.com/doi/abs/10.1002/(SICI)1099-1085(199801)12:1%3C105::AID-HYP566%3E3.0.CO;2-%23

Gulley, J. D., Grabiec, M., Martin, J. B., Jania, J., Catania, G., & Glowacki, P. (2012). The effect of discrete recharge by moulins and heterogeneity in flow-path efficiency at glacier beds on subglacial hydrology. *Journal of Glaciology*, *58*(211), 926–940. https://doi.org/10.3189/2012JoG11J189

Herring, T., King, R. W., & McClusky, S. C. (2010). *Introduction to GAMIT/GLOBK*. Cambridge, MA: Massachusetts Institute of Technology.

Hoffman, M. J., Andrews, L. C., Price, S. F., Catania, G. A., Neumann, T. A., Lüthi, M. P., et al. (2016). Greenland subglacial drainage evolution regulated by weakly connected regions of the bed. *Nature Communications*, *7*, 13903. https://doi.org/10.1038/ncomms13903

Hoffman, M. J., Catania, G. A., Neumann, T. A., Andrews, L. C., & Rumrill, J. A. (2011). Links between acceleration, melting, and supraglacial lake drainage of the western Greenland Ice Sheet. *Journal of Geophysical Research*, *116*(4), 1–16. https://doi.org/10.1029/2010JF001934

Hoffman, M. J., Perego, M., Andrews, L. C., Catania, G. A., Price, S. F., Lüthi, M. P., et al. (2018). Widespread moulin formation during supraglacial lake drainages in Greenland. *Geophysical Research Letters*, *45*, 778–788. https://doi.org/10.1002/2017GL075659

Iken, A., & Truffe, M. (1997). The relationship between subglacial water pressure and velocity of Findelengletscher, Switzerland, during its advance and retreat. *Journal of Glaciology*, *43*(144), 328–338. https://doi.org/10.1017/s0022143000003282

Joughin, I., Das, S. B., Flowers, G. E., Behn, M. D., Alley, R. B., King, M. A., et al. (2013). Influence of ice-sheet geometry and supraglacial lakes on seasonal ice-flow variability. *The Cryosphere*, *7*, 1185–1192. https://doi.org/10.5194/tc-7-1185-2013

Lliboutry, L. A. (1968). Local friction laws for glaciers: A critical review and new openings. *Journal of Glaciology*, *23*(89), 67–95.

Meierbachtol, T. W., Harper, J. T., & Humphrey, N. F. (2013). Basal drainage system response to increasing surface melt on the Greenland ice sheet. *Science*, *341*(6147), 777–779. https://doi.org/10.1126/science.1235905

Meierbachtol, T. W., Harper, J. T., Humphrey, N. F., & Wright, P. J. (2016). Mechanical forcing of water pressure in a hydraulically isolated reach beneath Western Greenland's ablation zone. *Annals of Glaciology*, *57*(72), 62–70. https://doi.org/10.1017/aog.2016.5

Mejia, J. Z., Gulley, J. D., & Dixon, T. H. (2020). *West Greenland moulins 2017–2019 Sermeq Avannarleq—GPS/GNSS observations dataset*. The GAGE Facility operated by UNAVCO, Inc. https://doi.org/10.7283/VT31-EK40

Mejia, J. Z., Trunz, C., Covington, M. D., & Gulley, J. D. (2020). *Meteorological data from two on-ice weather stations at 780 and 950 MASL elevations in the ablation area of Sermeq Avannarleq, West Greenland from 2017–2018*. Arctic Data Center. https://doi.org/10.18739/A2CF9J745

Mejia, J. Z., Trunz, C., Covington, M. D., Gulley, J. D., & Breithaupt, C. (2020). *Moulin hydrological measurements from Sermeq Avannarleq, West Greenland Ice Sheet from 2017–2018*. Arctic Data Center. https://doi.org/10.18739/A2M03XZ13

Mejia, J. Z., Trunz, C., Gulley, J. D., & Covington, M. D. (2021). *Surface meltwater production timeseries for Sermeq Avannarleq, western Greenland Ice Sheet from 2017–2018*. Arctic Data Center. https://doi.org/10.18739/A2V97ZS6G

Morlighem, M., Williams, C. N., Rignot, E., An, L., Arndt, J. E., Bamber, J. L., et al. (2017). BedMachine v3: Complete bed topography and ocean bathymetry mapping of Greenland from multibeam echo sounding combined with mass conservation. *Geophysical Research Letters*, *44*(21), 11051–11061. https://doi.org/10.1002/2017GL074954

Morriss, B. F., Hawley, R. L., Chipman, J. W., Andrews, L. C., Catania, G. A., Hoffman, M. J., et al. (2013). A ten-year record of supraglacial lake evolution and rapid drainage in West Greenland using an automated processing algorithm for multispectral imagery. *The Cryosphere*, *7*(6), 1869–1877. https://doi.org/10.5194/tc-7-1869-2013

Murray, T., & Clarke, G. K. C. (1995). Black-box modeling of the subglacial water system. *Journal of Geophysical Research*, *100*(B7), 10231–10245. https://doi.org/10.1029/95jb00671

Rada, C., & Schoof, C. (2018). Channelized, distributed, and disconnected: Subglacial drainage under a valley glacier in the Yukon. *The Cryosphere*, *12*(8), 2609–2636. https://doi.org/10.5194/tc-12-2609-2018

Roeoesli, C., Helmstetter, A., Walter, F., & Kissling, E. (2016). Meltwater influences on deep stick-slip icequakes near the base of the Greenland Ice Sheet. *Journal of Geophysical Research: Earth Surface*, *121*, 223–240. https://doi.org/10.1002/2015JF003601

Schoof, C. (2010). Ice-sheet acceleration driven by melt supply variability. *Nature*, *468*(7325), 803–806. https://doi.org/10.1038/nature09618

Schwanghart, W., & Kuhn, N. J. (2010). TopoToolbox: A set of Matlab functions for topographic analysis. *Environmental Modelling & Software*, *25*(6), 770–781. https://doi.org/10.1016/j.envsoft.2009.12.002

Selmes, N., Murray, T., & James, T. D. (2011). Fast draining lakes on the Greenland Ice Sheet. *Geophysical Research Letters*, *38*(15), 1–5. https://doi.org/10.1029/2011GL047872

Sole, A. J., Mair, D. W., Nienow, P. W., Bartholomew, I., King, M. A., Burke, M. J., & Joughin, I. (2011). Seasonal speedup of a Greenland marine-terminating outlet glacier forced by surface melt-induced changes in subglacial hydrology. *Journal of Geophysical Research*, *116*(3), 1–11. https://doi.org/10.1029/2010JF001948

Sole, A. J., Nienow, P. W., Bartholomew, I., Mair, D. W., Cowton, T., Tedstone, A. J., & King, M. A. (2013). Winter motion mediates dynamic response of the Greenland Ice Sheet to warmer summers. *Geophysical Research Letters*, *40*(15), 3940–3944. https://doi.org/10.1002/grl.50764

Steffen, K., Box, J. E., & Abdalati, W. (1996). *Greenland climate network: GC-Net*, US Army Cold Regions Reattach and Engineering (CRREL), CRREL Special Report(pp. 98–103). Cold Regions Research and Engineering Laboratory, CRREL Spec.

Stevens, L. A., Behn, M. D., McGuire, J. J., Das, S. B., Joughin, I., Herring, T., et al. (2015). Greenland supraglacial lake drainages triggered by hydrologically induced basal slip. *Nature*, *522*(7554), 73–76. https://doi.org/10.1038/nature14480

Stone, D., & Clarke, G. (1996). In situ measurements of basal water quality and pressure as an indicator of the character of subglacial drainage systems. *Hydrological Processes*, *10*(4), 615–628.

Sundal, A. V., Shepherd, A., Nienow, P. W., Hanna, E., Palmer, S., & Huybrechts, P. (2011). Melt-induced speed-up of Greenland ice sheet offset by efficient subglacial drainage. *Nature*, *469*(7331), 521–524. https://doi.org/10.1038/nature09740

Virtanen, P., Gommers, R., Oliphant, T. E., Haberland, M., Reddy, T., Cournapeau, D., et al. (2020). SciPy 1.0: Fundamental algorithms for scientific computing in Python. *Nature Methods*, *17*(3), 261–272. https://doi.org/10.1038/s41592-019-0686-2

Walder, J. S. (1986). Hydraulics of subglacial cavities. *Journal of Glaciology*, *32*(112), 439–445. https://doi.org/10.1017/s0022143000012156

Williamson, A. G., Arnold, N. S., Banwell, A. F., & Willis, I. C. (2017). A fully automated supraglacial lake area and volume tracking ("FAST") algorithm: Development and application using MODIS imagery of West Greenland. *Remote Sensing of Environment*, *196*, 113–133. https://doi.org/10.1016/j.rse.2017.04.032

Xie, S., Law, J., Russell, R., Dixon, T. H., Lembke, C., Malservisi, R., et al. (2019). Seafloor geodesy in shallow water with GPS on an anchored spar buoy. *Journal of Geophysical Research: Solid Earth*, *124*(11), 12116–12140. https://doi.org/10.1029/2019JB018242

Supporting Information for "Isolated cavities dominate Greenland Ice Sheet dynamic response to lake drainage"

DOI: 10.1002/2021GL094762

J. Z. Mejía[1,2], J. D. Gulley[1], C. Trunz[3,4], M. D. Covington[3], T. C. Bartholomaus[5], S. Xie[6], T. Dixon[1]

[1]Department of Geosciences, University of South Florida, Tampa, FL 33620
[2]Department of Geology, University at Buffalo, Buffalo, NY 14260
[3]Department of Geosciences, University of Arkansas, Fayetteville, AR 72701
[4]Department of Applied Geomatics, Université de Sherbrooke, Sherbrooke, QC J1K 2R1 Canada
[5]Department of Geological Sciences, University of Idaho, Moscow, ID 83844
[6]Scripps Institution of Oceanography, University of California San Diego, La Jolla, CA 92093

Contents of this file

Introduction
Text S1: Subglacial routing via hydropotential gradients
Text S2: Moulin instrumentation
Text S3: GNSS station data collection and processing
Text S4: Ice uplift
Text S5: Seismic analysis
Text S6: Supraglacial lake volumes
Text S7: 2017 lake drainage event
Text S8: Meltwater production
Figures S1 to S10
Tables S1 to S3

Introduction

This supplement provides additional information relating to the main text and details on methodology. **Text S1** describes the calculation of subglacial hydraulic potential gradients used to estimate subglacial routing in the Paakitsoq area of Sermeq Avannarleq. **Text S2** elaborates on moulin instrumentation, errors, and corrections for atmospheric pressure variability. **Text S3** describes methods used in processing GNSS station data, calculating ice velocities, and **Text S4** describes uplift determination used in **Figure 3d**. **Text S5** elaborates on the procedure used to determine glaciohydraulic tremor amplitude and icequake occurrence detected by the SELC seismic station. **Text S6** describes the area-to-volume scaling relationship used to estimate supraglacial lake volumes reported in **Table S2**. We describe the 2017 drainage of supraglacial lakes A and B is in **Text S7**. Finally, in **Text S8** we describe the calculation of supraglacial meltwater production shown in **Figure S8**.

Table S1 contains the coordinates of our instruments and provides a brief site description. **Table S2** describes the supraglacial lakes whose drainage was captured during the 2017 and 2018 melt seasons (e.g., **Figures 1, S1, S7, and S9**). We provide the coordinates, elevations, and local ice thicknesses of each lake. We also provide an estimate of the maximum area obtained by each supraglacial lake prior to drainage that was determined using satellite imagery before the 2017 and 2018 drainages. We use these areas to estimate the volume of water contained within each lake by applying an area-to-volume scaling relationship. **Table S3** describes wintertime background velocities determined for each of our three GNSS stations and provides the date ranges used in their determination (see **Text S3**).

Figure S4 is shows an extended timeseries of moulin hydraulic head, glaciohydraulic tremor amplitude, and ice velocity **Figure 2**. **Figure S5** shows the relationship between moulin hydraulic head and ice velocity. **Figure S7** shows the satellite imagery constraints on the July 2018 lake drainage event.

Text S1. Subglacial routing via hydraulic potential gradients

We estimate subglacial hydraulic potential gradients (ϕ) following:

$$\phi = \rho_w g z_b + P_w \tag{1}$$

where ρ_w is the density of water, g is acceleration due to gravity, z_b is bed elevation, and P_w is subglacial water pressure, assumed to be equal to ice overburden pressure (or $\rho_i g h$, where ρ_i is ice density and h is the ice thickness). Surface and bed elevations (**Figure S2**) are derived from the BedMachine Greenland v3 (Morlighem et al., 2017) with a 150 m resolution. This calculation requires the assumption that subglacial water pressures are at overburden throughout the domain during conduit formation. Once conduit flow paths are established, they can expand by melting and contract by creep closure but their locations are unlikely to change (Gulley et al., 2012). We determine flow paths by calculating flow accumulation along subglacial hydraulic potential gradients using the MATLAB Topotools toolbox (Schwanghart & Kuhn, 2010). We use surface and bed elevations at points spaced 50 m along the hydraulic potential flow path connecting Lake E to the terminus (bold cyan line) for the bed profile in **Figure 1c**.

While our observations show a direct connection between a draining supraglacial lake and a moulin located over 8 km downglacier, instrument records suggest the floodwave modified an even larger area of the subglacial drainage system. The similarity between the GNSS station response to each lake drainage event indicates the lateral extent of the floodwave was at least 500 m, which is approximately equivalent to the ice thickness in this area. We argue that our observations reflect the lower limit on the area of the isolated drainage system dewatered by the subglacial floodwave. It is likely that similar alterations to the subglacial drainage system occurred at downglacier locations as the floodwave continued propagating towards the coast.

Copyright 2021 by the American Geophysical Union.
0094-8276/21/$5.00

Text S2. Moulin instrumentation

Moulins were instrumented by lowering measured lengths of cable until the sensor reading increased with water depth, indicating we reached the water column within the moulin shaft (Mejia, Trunz, et al., 2020). We then continued lowering the sensor while confirming depth increases. Upon encountering features where feeding more cable into the moulin did not change the sensor's recorded depth, we anchored the cable to the ice surface. We fixed the sensor in place within PIRA moulin at 154.5 m below the ice surface. We recorded water pressures every 15-min with Campbell Scientific CR-1000 data loggers equipped with AVW200 modules.

To convert the piezometer's measurements of water pressure (P_w) to hydraulic head (h) we subtract the piezometer's depth from the GNSS reported ice surface elevation to determine the sensor elevation (z_{sensor}) in meters above sea level. Because the uppermost $\sim$ 30 m of the moulin's shaft appeared vertical, we calculate hydraulic head (h) using:

$$h = \frac{P_w}{\rho_w g} + z_{sensor} \tag{2}$$

where ρ_w is the density of water and g is acceleration due to gravity. We estimate an error of 20 m in our absolute moulin head measurements, arising from the uncertainty in the sensor elevation as described in detail in Andrews et al. (2014). Importantly, error in absolute moulin head does not apply to our measurements of relative change (e.g. diurnal variations). We represent moulin hydraulic head as measured from sea-level to allow for comparison with existing data sets and to avoid using poorly constrained bed elevations which have associated uncertainties on the order of $\pm$ 100 m.

We use atmospheric pressures recorded by the Greenland Climate Network (GC-NET) weather station JAR1 (Steffen et al., 1996), located approximately 5 km northeast of our instrumented moulins JEME (2017) and PIRA (2018). Due to instrument failure, atmospheric pressure variations were not available during the 2018 melt season to correct our timeseries of moulin water level for atmospheric pressure variability. However, the additional error introduced to our 2018 water pressure record is likely small as evidenced by the 2017 correction (**Figure S2**) where atmospheric pressure variability is on the order of centimeters (standard deviation, std=0.05 m) while moulin hydraulic head variability is on the order of tens of meters (std=34.5 m).

The Geokon piezometers that we used to instrument moulins in 2017 and 2018 were also equipped with temperature sensors that monitored water temperatures throughout the instrumentation. We plot the piezometer's recorded temperature before, during, and after the 2018 lake drainage in **Figure S8c**. This timeseries shows that under typical melt-driven diurnal moulin water level fluctuations, the temperature recorded by the piezometer increases with moulin water level as the supraglacial meltwater mixes and raises the moulin's water column to submerge the sensor. On 25 July 2018, surface derived meltwater entering the moulin raises the water temperatures, following the normal pattern. However, at the start of the lake drainage event—described in the main text, Section 3—as moulin water level jumps in response to the incoming subglacial floodwave, water temperature drops sharply. This drop in water temperature indicates that the influx of water originated at the moulin's base, pushing up the water column and exposing the piezometer to colder water that was previously deeper in the column. The cold temperatures following the lake drainage were caused by the piezometer no longer being submerged and by the concurrent drop in air temperatures. Ultimately, our calculations of hourly meltwater production derived from the LOWC weather station (**Figure S8a**; Mejia et al., 2021) do not indicate a high-magnitude melt event coincident with the lake drainages. Together, these observations confirm a subglacial source for the pressure pulse we identified as the subglacial floodwave following upglacier lake drainage events.

Text S3. GNSS station data collection and processing

We measured ice surface motion using three on-ice GNSS stations installed at Low Camp during July 2017 (**Figure 1, Table S1**). Each station was equipped with a Trimble NetR9 Receiver (30-s sampling rate) and a Zephyr Geodetic Antenna mounted onto aluminum conduit frozen over two meters into the ice surface. GNSS station JEME was co-located ($\sim$ 20 m) with the moulin JEME instrumented during the 2017 melt season. By July 2018, JEME moulin and GNSS station had been advected downglacier, resulting in the separation of JEME GNSS station and our instrumented moulin PIRA by $\sim$ 60 m. Alternatively, GNSS station LMID was located approximately 400 m south of the instrumented moulins and operated throughout the 2017 and 2018 melt seasons. GNSS station JNIH was located $\sim$ 700 m south of instrumented moulin JEME moulin and was active in 2017. For processing we used the UNAVCO maintained GNSS station KAGA with a baseline length of 28 km (Fahnestock & Truffer, 2006) and the station ROCK we established on bedrock northeast of our site with a baseline length of 36 km (**Figure S3**; Mejia, Gulley, & Dixon, 2020).

We determined kinematic site positions from our on-ice GNSS station with TRACK software (Herring et al., 2010) which uses carrier-phase differential processing relative to bedrock mounted base stations (KAGA and ROCK). Kinematic positions were estimated using 30-s intervals that matched our receiver sampling rates. To reduce multi-path we applied a 10° cutoff angle and used long baseline mode during processing. To minimize smoothing gaps at the boundaries of our daily observation files, we followed the approach of (Xie et al., 2019) such that we extend each observation file with 12-h of data from the surrounding days. Once processed we removed the overlapping time periods. The resulting timeseries has a formal error of 1–2 cm in the horizontal direction and 4–5 cm vertically.

Post-processed positions were then imported to Python for further analysis (Virtanen et al., 2020). We transformed the position timeseries into the along-flow and across-flow directions for each station. Before calculating velocities, we filtered positions to reduce spurious signals resulting from GNSS uncertainties by applying a centered 2-h rolling mean to the timeseries. We calculated ice surface velocities by down-sampling the position timeseries from the 30-s receiver sampling rate to 3-m, before differencing 2-h separated positions. This analysis produced ice surface velocity timeseries with a 3-m sampling interval with an associated uncertainty of 0.024 m d^{-1}.

Following Hoffman and others (2011), we calculate three along-flow velocity timeseries using centered mean filters that emphasize variability on seasonal, diurnal, and event timescales. For seasonal timescales we apply a centered 24-h window which eliminates diurnal velocity fluctuations (**Figure S4**). For diurnal timescales we apply a centered 6-h window that emphasizes diurnal variability (**Figures 2c, S4, S5, and S10**). For the short timescales associated with the lake drainage event we use a 2-h window (**Figure 3c**). This 2-h window reduces attenuation at the beginning and end of the lake drainage event but does not eliminate it

completely. For this reason, we use the along-flow position timeseries to confirm the timing of the velocity response to the short-duration lake drainage event (**Figure 3b**).

We define winter background speed as the mean sliding speed over the longest period of continuous GNSS station operation before the onset of melting (6 June 2018). Accordingly, winter background speeds were determined using data from late May (**Table S3**), which is shown in **Figure S4d**.

Text S4. Ice uplift

Measured vertical ice motion is attributed to a combination of flow along a sloping bed, strain thickening or thinning, and bed separation caused by cavity opening or till dilation where subglacial sediments are present (Howat et al., 2008). To account for changes in elevation associated with bed slope, we detrend the vertical component of motion with respect to distance traveled in the along-flow direction using the linear fit before the melt season when strain and cavity opening should be constant (i.e., during the period termed "winter background"). We transform detrended vertical motion back to the time domain to produce the uplift timeseries shown in **Figure 3b**. The resultant uplift timeseries accounts for bed separation due to cavity opening, strain thickening or thinning, and sediment dilation. Previous studies close to our field site (Andrews et al., 2014; Hoffman et al., 2011) have also documented significant bed separation over short timescales, suggesting the uplift due to cavity growth likely significantly contributed to the more than 10 cm of ice surface uplift observed by our GNSS stationsduring each lake drainage event. Because ice thickness in this area is poorly constrained ($\pm$100 m), our estimates of ice overburden pressure have enough uncertainty that subglacial water pressures may have reached or exceeded overburden when the subglacial floodwave past our site. Accordingly, some of the observed uplift may have been caused by hydraulic jacking at the ice-sheet's bed.

Text S5. Seismic analysis

We deployed a seismic station approximately 150 m away from PIRA moulin in April 2018 to record local icequakes and seismic glaciohydraulic tremor amplitude, a proxy for the flux of subglacial discharge (Bartholomaus et al., 2015). This station was equipped with a Nanometrics Centaur digitizer connected to a Nanometrics Trillium Compact Posthole sensor re-installed on 12 July 2018, 1.1 m below the ice surface. We poured sand over the top of the seismometer at the time of installation to improve coupling between the sensor and surrounding ice. Ablation measurements from late July 2018 indicate that the sensor remained at least 0.5 m below the ice surface when subglacial floodwaters passed beneath the sensor.

Glaciohydraulic tremor is characterized by long-duration, low amplitude background seismic noise that varies slowly without clear onset or termination. The amplitude of these ground variations depends on both the flux and the pressure gradient of turbulently-flowing water within efficient, well-connected conduits. We characterized the glaciohydraulic tremor amplitude using two different metrics: (1) the median power between 1.5–10 Hz calculated within hourly data windows (Bartholomaus et al., 2015), and (2) as the 20th percentile amplitude of enveloped, 10-m, seismic waveforms, high-pass filtered above 2 Hz. This 20th percentile amplitude was chosen to be well below the higher percentile values that may represent distinct ice fracturing events-equivalent results are obtained for other percentile metrics below approximately fifty. Because both measures of glaciohydraulic tremor produced qualitatively similar timeseries, but the second approach was tailored to work with better temporal resolution, we present the 20th percentile envelope analysis.

Distinct from the slowly varying timeseries of glaciohydraulic tremor are distinct, impulsive "icequakes" that typically are found at frequencies greater than 10 Hz. These icequakes are produced by ice fracture events (e.g., crevassing) at the glacier surface, englacially, or at the glacier bed. We quantify the strength of these locally recorded seismic events by the maximum seismic amplitude recorded at our station within 10-min moving windows. The maximum seismic amplitude depends both on the scale of an event (slip length, stress reduction during the event, and surface area of the fracture surface) and the distance between the event origin and the sensor. Thus the seismic amplitude time series (**Figure 3f**) reveals information regarding the proximity and intensity of fracturing events near our instrumentation site.

To better understand the origin of the peak seismic amplitudes that follow the peak in tremor amplitude, we manually examined the seismic waveforms themselves. These waveforms include many, frequent, large-amplitude icequakes. The six largest amplitude events on 25 July 2018, all occurring within two hours of the peak tremor amplitude (**Figure S6**). These events each consist of very sharp first arrivals on the vertical channels (consistent with *P*-waves) and weak or non-existent *S*-waves, very high frequency content (greater than 50 Hz and extending to the 250 Hz Nyquist frequency, indicating that the waveforms are undersampled), inter-phase arrival times that are consistent with a source 500–1000 m from the station (such as the bed), and mostly with downward first *P*-wave motions, consistent with some kind of crack closing. Some of these high frequency events had a low-frequency coda consistent with the presence of water. So, while we lack the ability to definitively locate these events, based on our observations and the similarity of these events to other events with basal origin (Röösli et al., 2014; Walter et al., 2013), we rule out an origin associated with near-surface crevassing and believe that the high-amplitude icequakes late on 25 July are well explained as ice fracture events at the ice sheet bed.

Text S6. Supraglacial lake volumes

Maximum lake extents prior to drainage were manually delineated and used with QGIS interactive measurement tools to perform an ellipsoidal calculation to find lake area. We use the most recent satellite imagery available from either Landsat or Sentinel products acquired before the lake drainage events in 2017 and 2018 (**Figures S7, S9**). Supraglacial lake extents are outlined in **Figures 1, S1, S7, and S9**. We use these areas to estimate the volume of water stored within each supraglacial lake. Lake volume estimates (reported in **Table S2**) are calculated using an area-to-volume scaling relationship for the Paakitsoq region of the GrIS (Williamson et al., 2017), where lake volume (V) in m^3 can be calculated following:

$$V = 575,341 \times A^2 + 271,187 \times A + 89,617 \qquad (3)$$

where A is the lake area in km^2. Calculated volumes have an associated error of 4.2×10^5 m^3. The numbers reported next to the lake names correspond with naming conventions used by Morriss et al. (2013). Maximum extent was determined using QGIS tools and a combination of Landsat-8 and Sentinel-2 imagery, courtesy of the U.S. Geological Survey.

Text S7. 2017 lake drainage event

On 21 July 2017, we instrumented JEME moulin with a pressure transducer that was anchored 350 m below the ice surface. By July 2018, moulin JEME had been advected 90 m downglacier, consistent with measured annual ice displacement of approximately 90 m a^{-1}. On 10 July 2018, we instrumented the new moulin, PIRA, which opened in the same position on the ice sheet as JEME the year before. In 2017, Sentinel 2 and Landsat 8 imagery captured two supraglacial lake drainages between 26–27 July (**Figure S9**; Lakes A and B; **Figure S10**). On 27 July at 02:30 UTC, moulin water levels deviated from their nightly decline as the subglacial floodwave created by the lake drainages approached our site. By 04:30 UTC, moulin water level had jumped more than 60 m (an increase of $\sim 13\%$ of ice overburden pressure) to peak levels of 671 m.a.s.l. (or $86 \pm 9\%$ of overburden pressure). The ice-dynamic response was similar at the LMID and JNIH GNSS stations. Peak moulin water level coincided with the peak along-flow ice velocities of 1.8 m d^{-1} and 2.0 m d^{-1} at stations LMID and JNIH, respectively, and peak vertical uplift of 14 ± 5 cm at both stations. After the subglacial floodwave drained past our site, the next day's ice velocity minimum dropped to winter background speeds. At the same time, moulin water level was still high, suggesting water pressure in the active drainage system was not responsible for the decline in ice velocity.

Over the week following the lake drainage event minimum moulin water levels declined. By 3 August, the diurnal minimum moulin water level was 60 m lower than after the lake drainage event when ice velocities initially fell to wintertime background speeds. Despite this significant reduction in minimum moulin water level—for comparison, during the lake drainage event moulin water levels increased by 60 m—minimum ice velocity remained at winter background speeds, unaffected by the falling pressures within the active drainage system. This observation contradicts the behavior expected if increased efficiency of the channelized drainage system slowed sliding speeds. Therefore, while increased pressurization of the active drainage system reduced basal traction to drive diurnal acceleration, declining pressures in the active drainage did not reduce minimum sliding speeds. Instead, these observations indicate the state of the isolated drainage system governed the lower limit of sliding speeds.

Text S8. Meltwater production

We calculate surface meltwater production at Low Camp using measurements of air temperature (T) and incoming short-wave solar radiation (G) recorded by the LOWC weather station (Mejia et al., 2021). Hourly melt rate (M) in mm w.e. h^{-1} (**Figure S7**) was calculated using the enhanced temperature-index model by Pellicciotti et al. (2005).

$$M = \begin{cases} \mathbf{TF}\ T + \mathbf{SRF}(1-\alpha)G & \text{if } T > T_T \\ 0 & \text{if } T \leq T_T \end{cases} \quad (4)$$

where T is air temperature in °C, G is incoming shortwave solar radiation in W m^{-2}, α is ice surface albedo, T_T is a threshold temperature under which no melting occurs (taken to be 0°C). **TF** is the temperature factor and **SRF** is the shortwave radiation factor that we set to 0.05 mm h^{-1} C^{-1} and 0.0094 m^2 $mmW^{-1}h^{-1}$ respectively. We set $\alpha = 0.69$ using the last recorded albedo measured by the GC-NET weather station JAR1 on 23 June 2018, before the station stopped recording (Steffen et al., 1996).

References

Andrews, L. C., Catania, G. A., Hoffman, M. J., Gulley, J. D., Lüthi, M. P., Ryser, C., ... Neumann, T. A. (2014). Direct observations of evolving subglacial drainage beneath the Greenland Ice Sheet. *Nature*, *514*(7520), 80–83. doi: 10.1038/nature13796

Bartholomaus, T. C., Larsen, C. F., Amundson, J. M., O'Neel, S., Walter, J. I., & West, M. E. (2015). Subglacial discharge at tidewater glaciers revealed by seismic tremor. *Geophysical Research Letters*, *42*, 6391–6398. doi: 10.1002/2015GL064590

Fahnestock, M. A., & Truffer, M. (2006). *Greenland GNSS Network - KAGA-Kangia North P.S.,*. UNAVCO. doi: 10.7283/FQGY-4535

Gulley, J. D., Grabiec, M., Martin, J. B., Jania, J., Catania, G. A., & Glowacki, P. S. (2012). The effect of discrete recharge by moulins and heterogeneity in flow-path efficiency at glacier beds on subglacial hydrology. *Journal of Glaciology*, *58*(211), 926–940. doi: 10.3189/2012JoG11J189

Herring, T., King, R. W., & McClusky, S. C. (2010). Introduction to GAMIT/GLOBK. *Mass. Inst. of Technol., Cambridge, Mass*.

Hoffman, M. J., Catania, G. A., Neumann, T. A., Andrews, L. C., & Rumrill, J. A. (2011). Links between acceleration, melting, and supraglacial lake drainage of the western Greenland Ice Sheet. *Journal of Geophysical Research: Earth Surface*, *116*(4), 1–16. doi: 10.1029/2010JF001934

Howat, I. M., Tulaczyk, S. M., Waddlngton, E. D., & Björnsson, H. (2008). Dynamic controls on glacier basal motion inferred from surface ice motion. *Journal of Geophysical Research*, *113*(F3), F03015. doi: 10.1029/2007JF000925

Mejia, J. Z., Gulley, J. D., & Dixon, T. H. (2020). *West Greenland Moulins 2017-2019 Sermeq Avannarleq - GPS/GNSS Observations Dataset.* The GAGE Facility operated by UNAVCO, Inc. doi: 10.7283/VT31-EK40

Mejia, J. Z., Trunz, C., Covington, M. D., Gulley, J. D., & Breithaupt, C. (2020). *Moulin hydrological measurements from Sermeq Avannarleq, West Greenland Ice Sheet from 2017-2018.* Arctic Data Center. doi: 10.18739/A2M03XZ13

Mejia, J. Z., Trunz, C., Gulley, J. D., & Covington, M. D. (2021). *Surface meltwater production time-series for Sermeq Avannarleq, western Greenland Ice Sheet from 2017-2018.* Arctic Data Center. doi: 10.18739/A2V97ZS6G.

Morlighem, M., Williams, C. N., Rignot, E., An, L., Arndt, J. E., Bamber, J. L., ... Zinglersen, K. B. (2017). BedMachine v3: Complete Bed Topography and Ocean Bathymetry Mapping of Greenland From Multibeam Echo Sounding Combined With Mass Conservation. *Geophysical Research Letters*, *44*(21), 11,051–11,061. doi: 10.1002/

2017GL074954

Morriss, B. F., Hawley, R. L., Chipman, J. W., Andrews, L. C., Catania, G. A., Hoffman, M. J., ... Neumann, T. A. (2013). A ten-year record of supraglacial lake evolution and rapid drainage in West Greenland using an automated processing algorithm for multispectral imagery. *Cryosphere*, *7*(6), 1869–1877. doi: 10.5194/tc-7-1869-2013

Pellicciotti, F., Brock, B., Strasser, U., Burlando, P., Funk, M., & Corripio, J. (2005). An enhanced temperature - index glacier melt model including the shortwave radiation balance : development and testing for Haut Glacier d'Arolla , Switzerland. *Journal of Glaciology*, *51*(175), 573 – 587. doi: 10.3189/172756505781829124

Röösli, C., Walter, F., Husen, S., Andrews, L. C., Lüthi, M. P., Catania, G. A., & Kissling, E. (2014). Sustained seismic tremors and icequakes detected in the ablation zone of the greenland ice sheet. *Journal of Glaciology*, *60*(221), 563–575. doi: 10.3189/2014JoG13J210

Schwanghart, W., & Kuhn, N. J. (2010). TopoToolbox: A set of Matlab functions for topographic analysis. *Environmental Modelling and Software*. doi: 10.1016/j.envsoft.2009.12.002

Steffen, C., Box, J. E., & Abdalati, W. (1996). Greenland Climate Network: GC-Net. *Cold Regions Research and Engineering Laboratory*, *CRREL Spec*, 98–103.

Virtanen, P., Gommers, R., Oliphant, T. E., Haberland, M., Reddy, T., Cournapeau, D., ... Vázquez-Baeza, Y. (2020). SciPy 1.0: fundamental algorithms for scientific computing in Python. *Nature Methods*, *17*, 261–272. doi: 10.1038/s41592-019-0686-2

Walter, F., Dalban Canassy, P., Husen, S., & Clinton, J. F. (2013). Deep icequakes: What happens at the base of alpine glaciers? *Journal of Geophysical Research: Earth Surface*, *118*(3), 1720-1728. doi: 10.1002/jgrf.20124

Williamson, A. G., Arnold, N. S., Banwell, A. F., & Willis, I. C. (2017). A Fully Automated Supraglacial lake area and volume Tracking ("FAST") algorithm: Development and application using MODIS imagery of West Greenland. *Remote Sensing of Environment*, *196*, 113–133. doi: 10.1016/j.rse.2017.04.032

Xie, S., Law, J., Russell, R., Dixon, T. H., Lembke, C., Malservisi, R., ... Chen, J. (2019). Seafloor Geodesy in Shallow Water With GPS on an Anchored Spar Buoy. *Journal of Geophysical Research: Solid Earth*, *124*(11), 12116–12140. doi: 10.1029/2019JB018242

Table S1. Field instrumentation locations.

		Coordinates			Ice	
	Type	Latitude	Longitude	Elevation	thickness	
		°N	°E	m.a.s.l.	m	
PIRA	Moulin	69.4741	-49.8232	779	503	Instrumented in 2018.
JEME	GNSS	69.4738	-49.8249	797	503	Co-located with JEME moulin in 2017, advected downglacier in 2018.
LMID	GNSS	69.4708	-49.8189	796	514	Uncrevassed, located between GNSS stations JEME and JNIH.
JNIH	GNSS	69.4684	-49.8318	790	547	Uncrevassed, near moulin JNIH.
LOWC	Weather	69.4727	-49.8263	777	512	Located 200 m south of PIRA moulin. Uncrevassed area with nearby supraglacial streams.
SELC	Seismic	69.4734	-49.8208	781	498	Installed April 2018. Uncrevassed area 150 m southeast of PIRA moulin.

Table S2. Supraglacial Lake coordinates and characteristics

	Max Area	Volume**	Latitude	Longitude	Elevation	Ice thickness	Distance (km)	
Lake	km^2	m^3	°N	°E	m.a.s.l.	m	Direct	Subglacial
A 63*	(0.633) 0.946	(4.9) 8.6×10^5	69.4537	-49.6247	888	728	7.4	8.9
B 59	(0.331) 0.362	(2.4) 2.6×10^5	69.4710	-49.6272	930	673	7.4	9.8
C 68	1.963	2.8×10^6	69.4355	-49.5297	913	882	12.3	13.4
D 57	0.490	3.6×10^5	69.4764	-49.3836	1021	918	17.4	22.2
E 50	1.365	1.5×10^6	69.4897	-49.2151	1100	1065	23.8	33.3
F 43	1.350	1.5×10^6	69.5343	-49.1291	1131	1120	27.9	40.2
G 45	0.493	3.6×10^5	69.5253	-49.1952	1159	1020	25.2	37.6
H 38	0.701	5.6×10^5	69.5496	-49.1801	1159	1100	26.5	40.6
I 35	2.300	3.8×10^6	69.5724	-49.2104	1146	1020	21.5	33.7
J 33	1.224	1.3×10^6	69.5680	-49.3410	1115	1160	26.4	37.6

* Naming convention used by (Morriss et al., 2013).

** Volume estimated using the Williamson and others (2017) area-to-volume scaling relationship for the Paakitsoq region. Values have an associated error of 0.420×10^6 m^3.

() Values associated with the 2017 lake drainage event.

Table S3. Winter background speed determination.

	Winter background speed ($m\ d^{-1}$)	Determined with data from dates
LMID	0.244	22–26 May 2018
JEME	0.240	21–26 May 2018
JNIH	0.258	21–26 May 2018

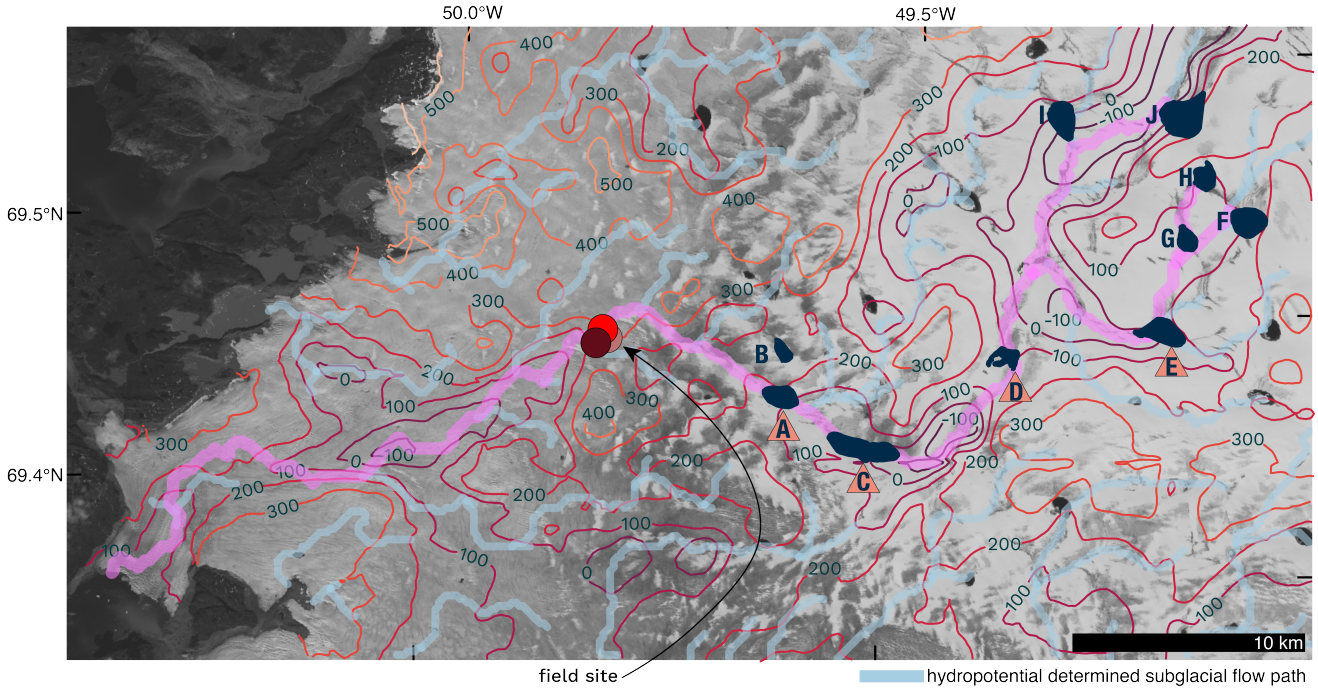


Figure S1. Bed topography and subglacial hydraulic potential used to predict subglacial flow routing. BedMachine v3 derived bed elevation contours are shown in meters. Subglacial flow routing from hydropotential gradients is shown in light blue. Supraglacial lakes mentioned in the main text are labeled and their maximum extents are marked in navy.

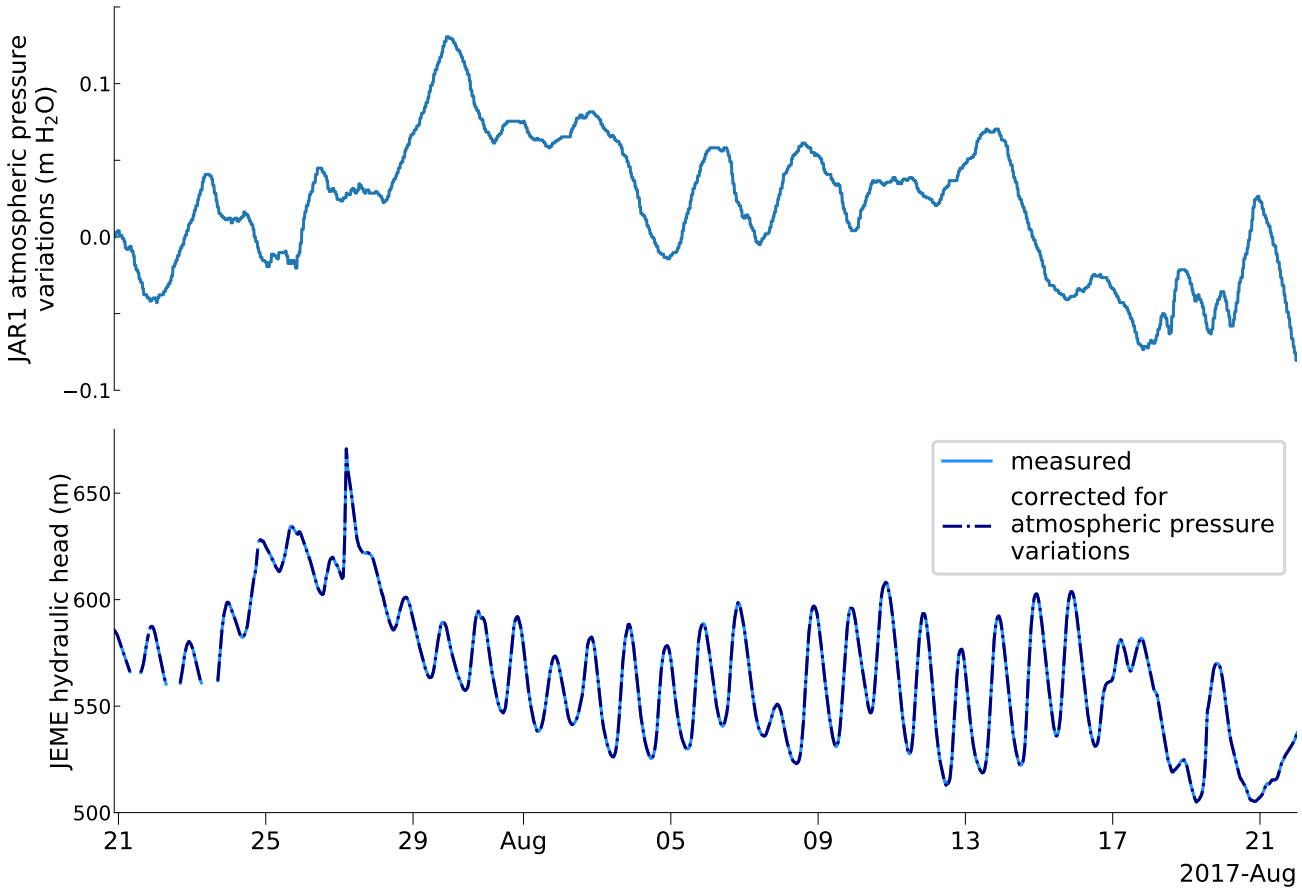


Figure S2. 2017 Atmospheric pressure variability. (a) Atmospheric pressure measured at JAR1 less the atmospheric pressure at the time JEME moulin was instrumented (9.2422 m H2O). (b) Hydraulic head measured at JEME moulin (blue), and moulin head corrected for atmospheric pressure variability shown in a, (navy dashed line).

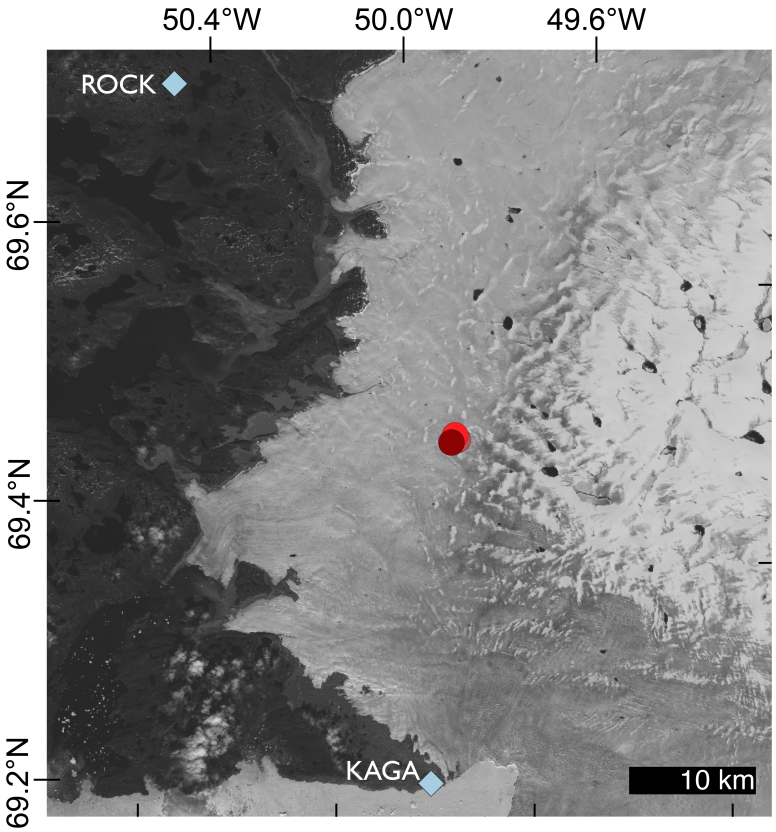


Figure S3. GNSS base station locations. Landsat imagery courtesy of the U.S. Geological Survey (21 July 2018). Base stations used in position determination. KAGA is located to the south of our study site, mounted on bedrock near the terminus of Sermeq Kujalleq (foreign name: Jakobshavn Isberæ). Our study area is marked by red circles.

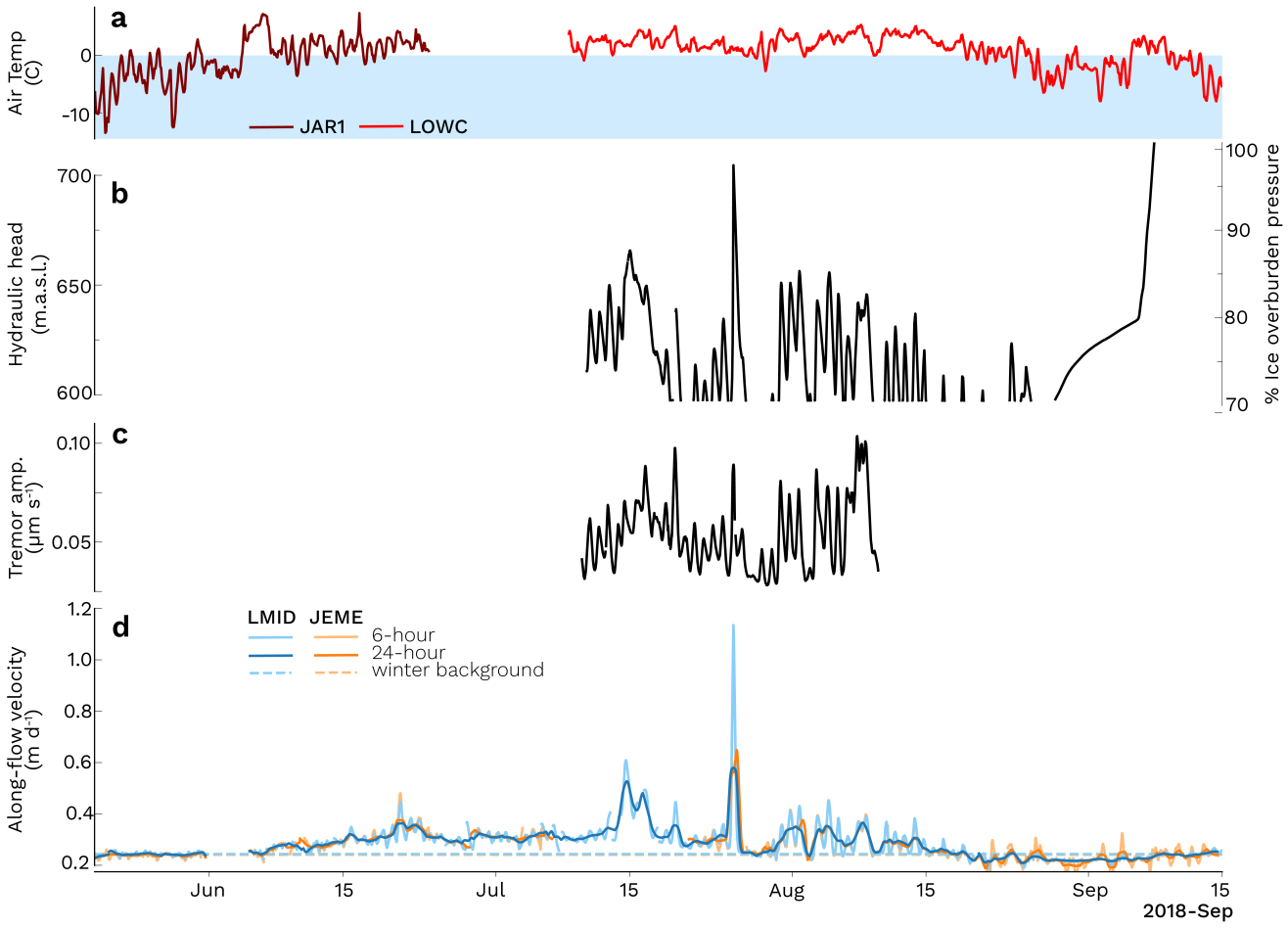


Figure S4. (a) Surface air temperature recorded at LOWC weather station (red) and the GC-NET station JAR1 (maroon). (b) Moulin hydraulic head in m.a.s.l. and fraction of overburden for an ice thickness of 503 m. (c) Glaciohydraulic tremor amplitude. (d) Along-flow ice velocity measured at stations JEME (orange) and LMID (blue). Light colors are smoothed with a 6-h centered rolling mean to show diurnal variability and light colors are smoothed with a 24-h rolling mean emphasize the slowdown following the mid-season lake drainage event. Dashed lines mark winter background sliding speeds for LMID and JEME.

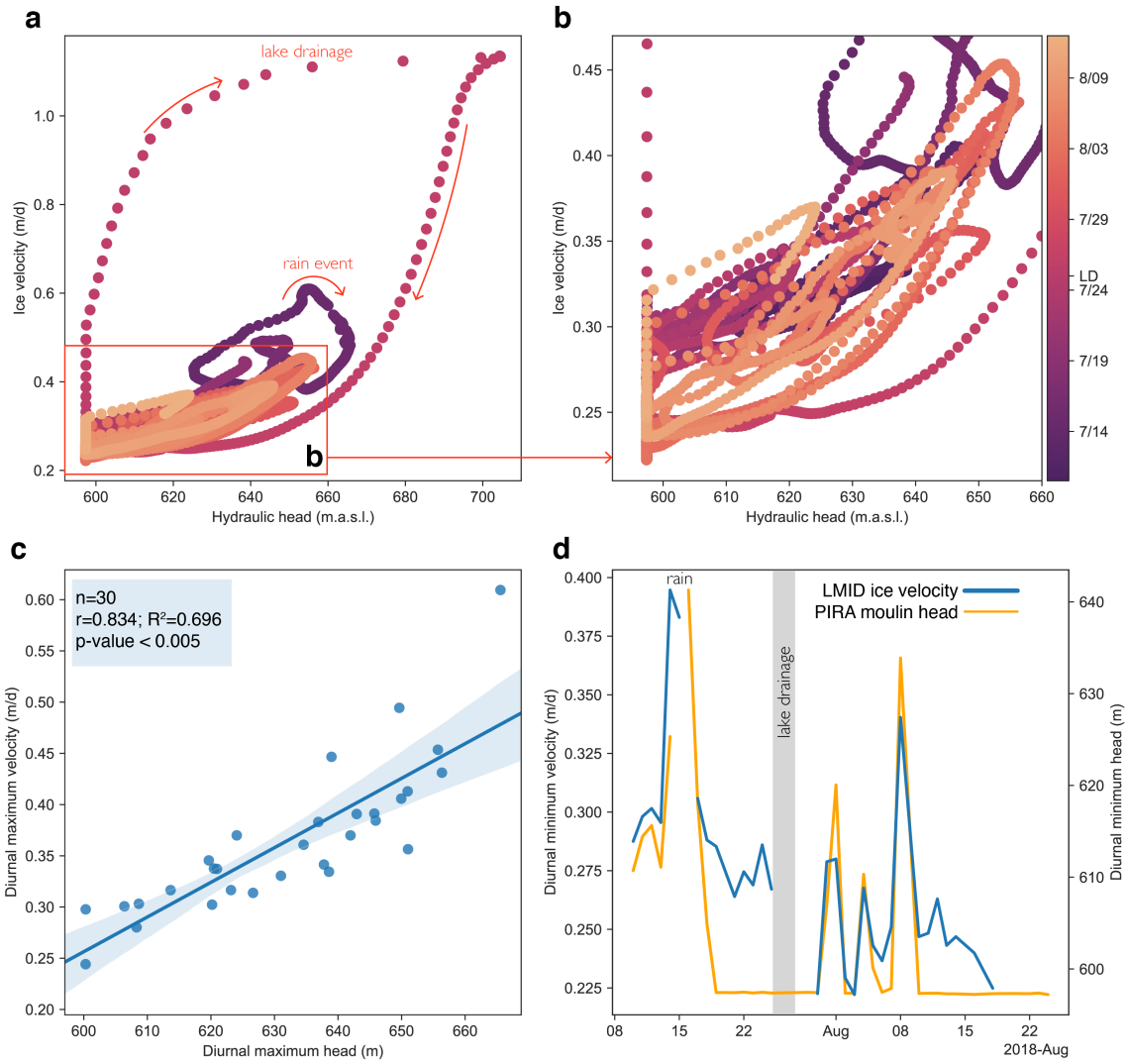


Figure S5. (a) Moulin hydraulic head and along-flow ice velocity (b) Zoomed in to show diurnal variations (lake drainage event is cropped). Colors indicate measurement date. Hydraulic head values are truncated to piezometer elevation (left). (c) Linear regression between daily maximum moulin hydraulic head and ice velocity ($n = 30$, $r = 0.834$, $p < 0.005$). (d) Moulin hydraulic head and ice velocity diurnal minimum values throughout the 2018 melt season.

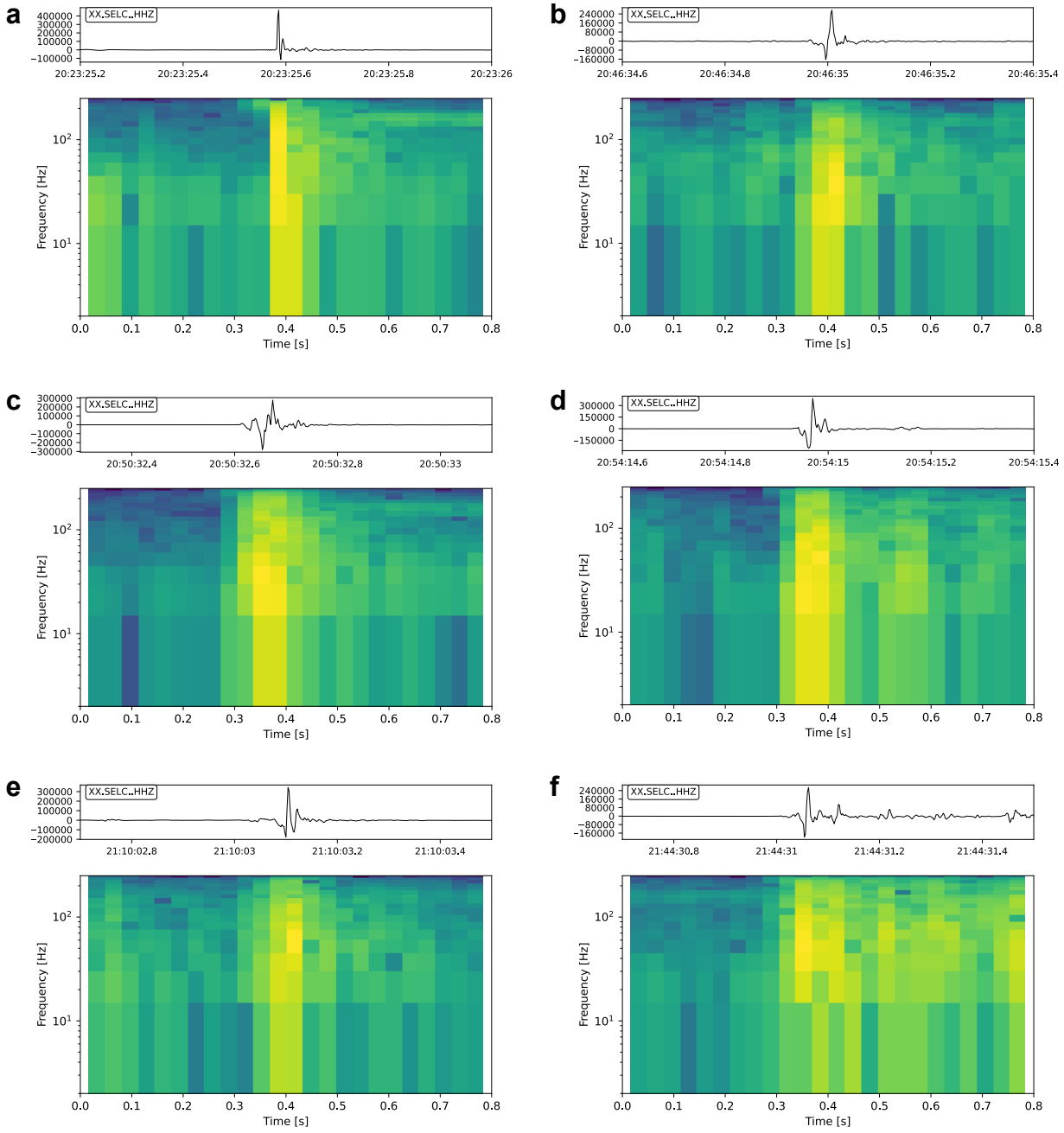


Figure S6. Waveforms and spectrograms of the six largest icequakes that occur after the interpretted passage of the subglacial flood water. For each of the six icequakes, the raw, vertical, seismic waveform is shown with units of counts (uncorrected for the instrument response, so as to minimally alter both the waveform and the relative timing of arrivals, and the frequency content of the events. Each panel shows 0.8 s of seismic data, with the icequake time in UTC on 25 July 2018. The relative scaling of y-axes for the waveforms vary amongst examples, as does the color scaling of the spectrograms (in dB ref. 1 counts^2/Hz)

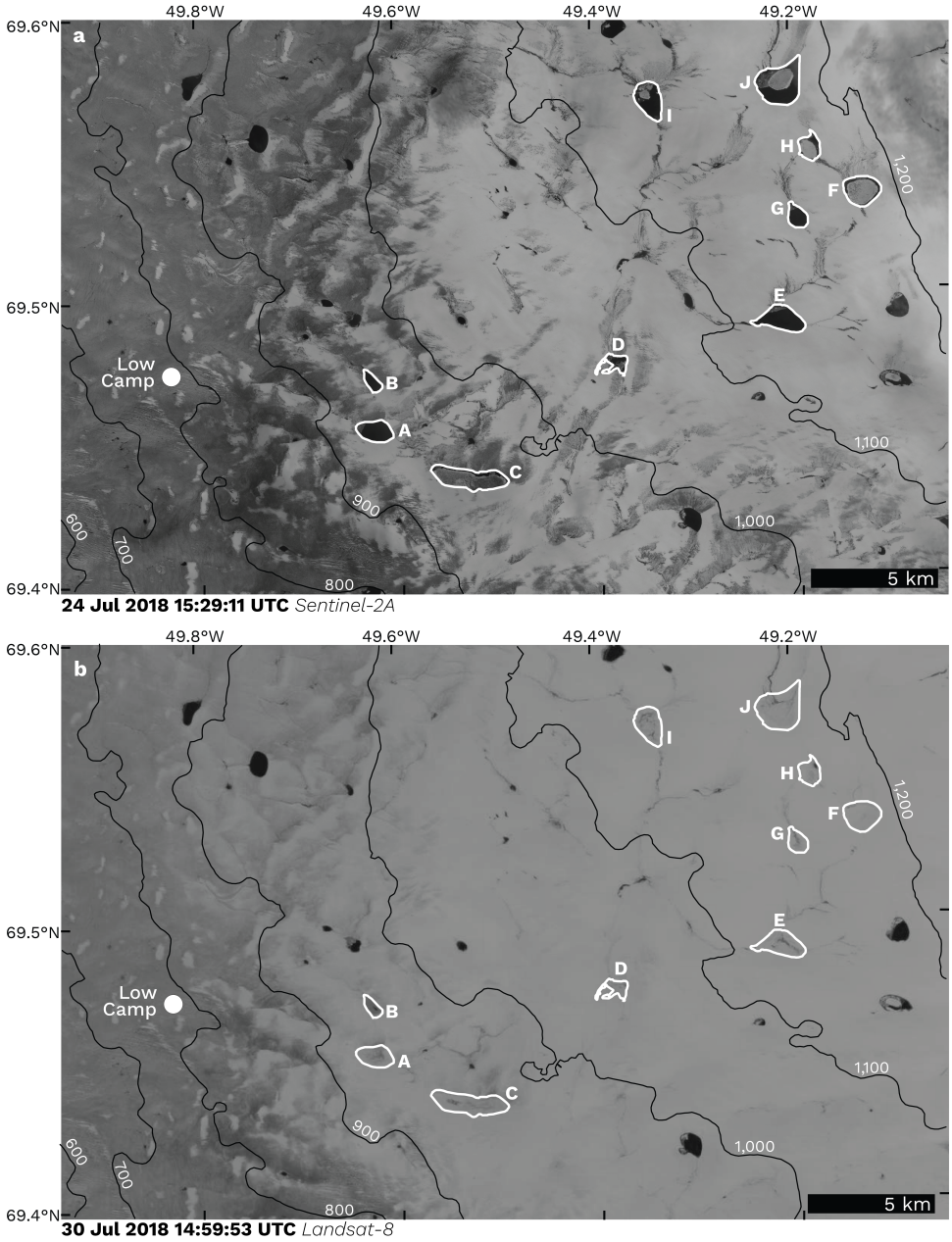


Figure S7. Satellite imagery constraints on 2018 lake drainage. (a) Copernicus Sentinel image acquired on 24 July 2018 at 15:29:11 UTC showing the maximum extents of supraglacial lakes A-J (red outlines), with the location of our instruments (red circles). (b) Landsat-8 image acquired on 30 July 2018 at 14:59:53 UTC showing the drainage of lakes A-J, maximum extents same as in a. Surface elevation contours from BedMachine v3. Data available from the U.S. Geological Survey

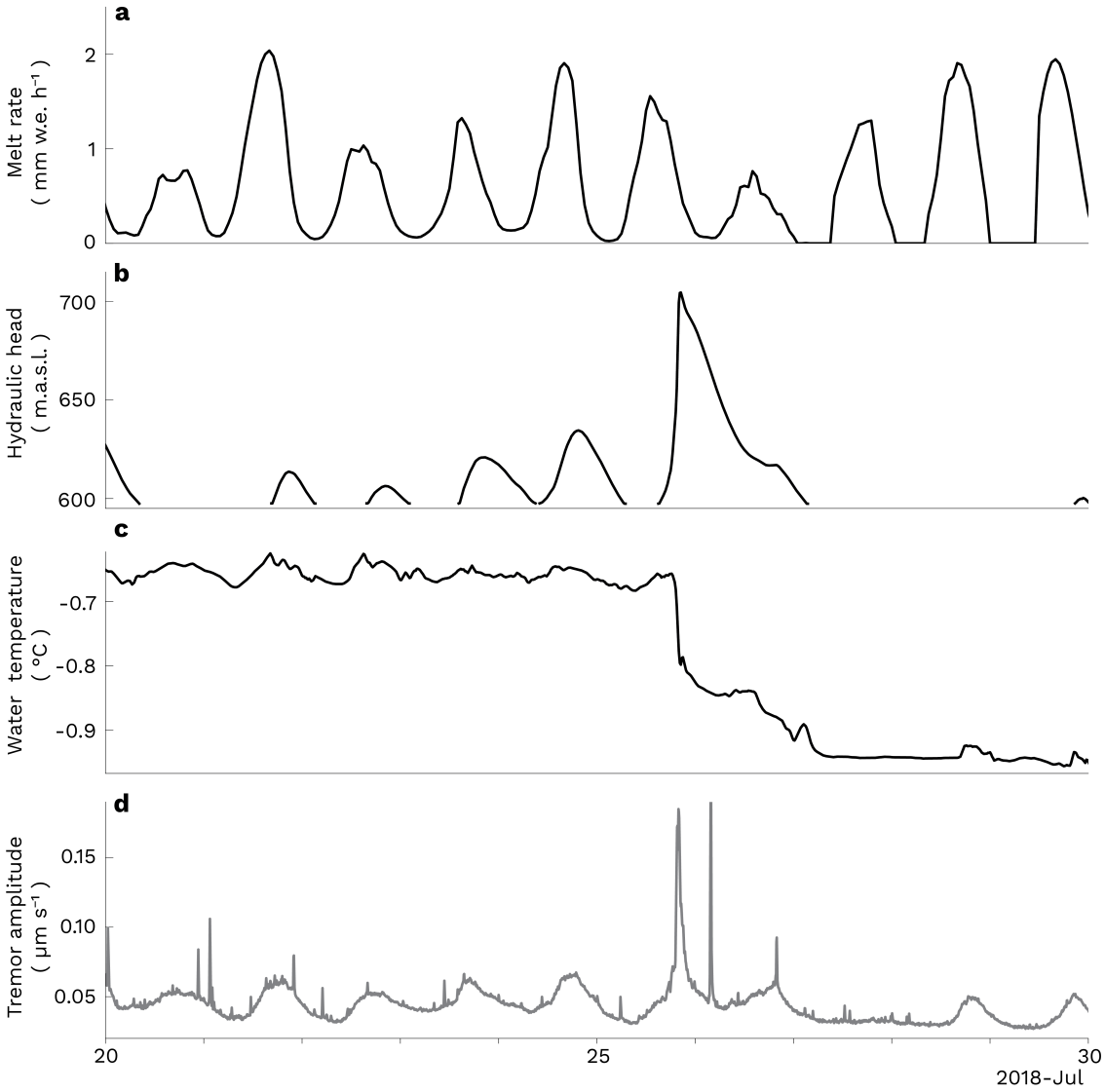


Figure S8. Surface meltwater production, moulin head and water temperature, and glaciohydraulic tremor amplitude comparison. (a) Hourly surface melt rate determined from the LOWC weather station. (b) PIRA moulin hydraulic head. (c) Hourly PIRA moulin water temperature. (d) Glaciohydraulic tremor amplitude.

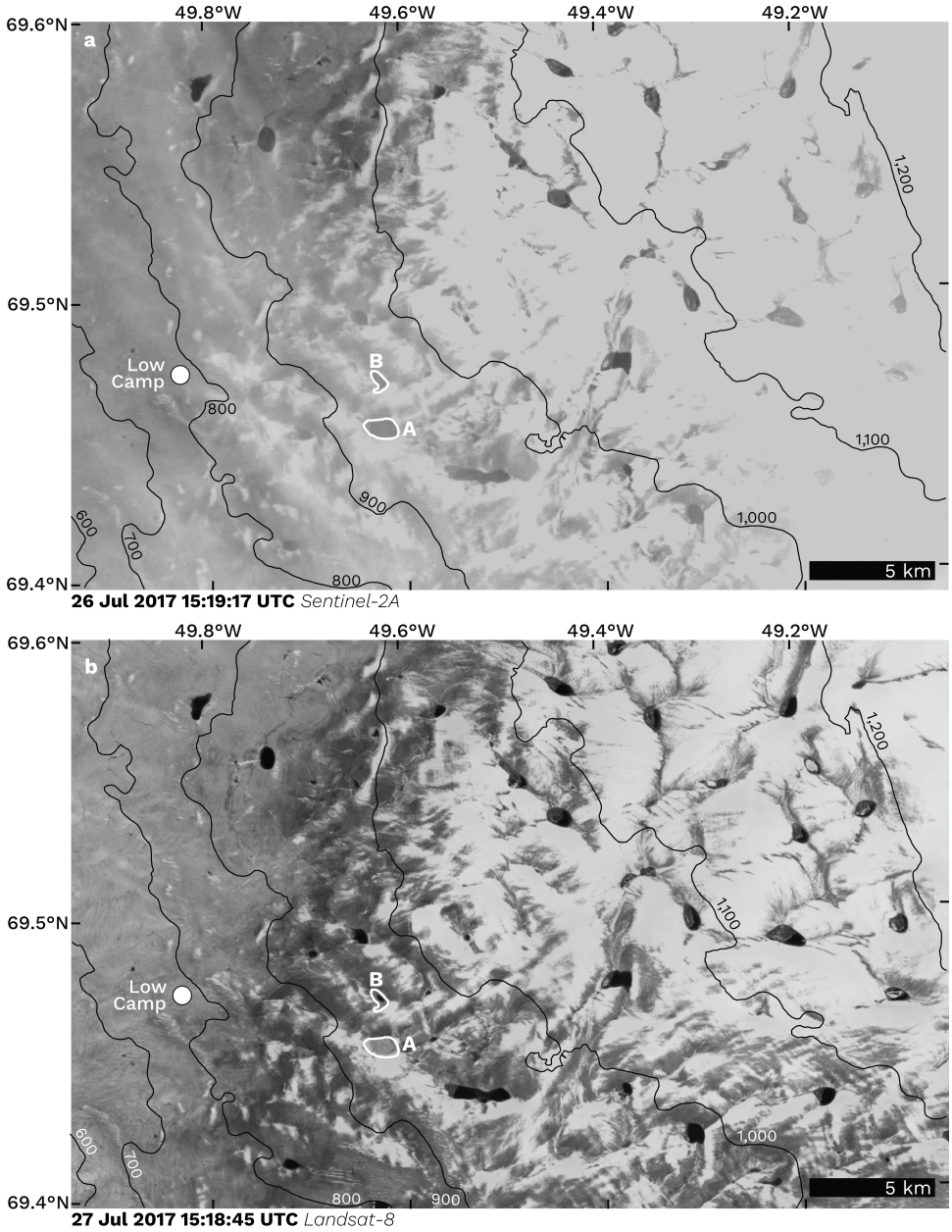


Figure S9. Satellite imagery constraints on 2017 lake drainages. (a) Sentinel-2A image from 26 July 2017 at 15:18:17 UTC showing the maximum extents of supraglacial lakes A and B (red), with the location of our instruments (red circles). (b) Landsat-8 image acquired on 27 July 2017 at 15:18:45 UTC showing the drainage of Lakes A and B, maximum extents same as in a. Surface elevation contours (m) are from BedMachine-v3.

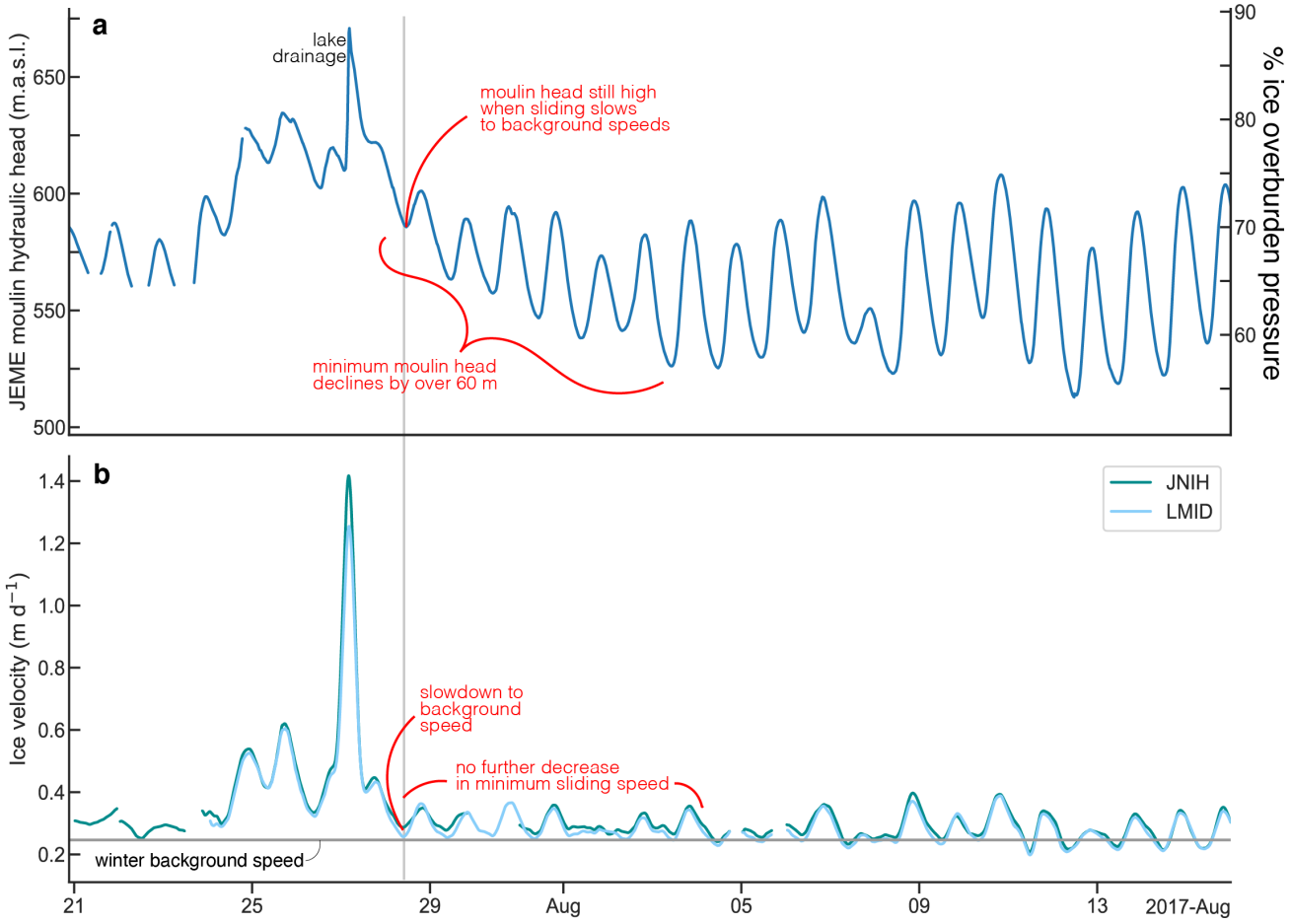


Figure S10. Moulin head and ice velocity timeseries showing 2017 lake drainage event. (a) JEME moulin hydraulic head (located in the same position as PIRA which formed in its place during early 2018). (b) Along-flow ice velocity from stations LMID (light blue) and JNIH (teal). This timeseries is interrupted by the passing of subglacial floodwaters on 28 July 2017. Sliding slows to winter background speeds (gray) despite high moulin head. Diurnal minimum moulin head falls over the subsequent week, amounting to 60 m (same magnitude as the lake drainage increase) but there is no further decrease in ice velocity as would be expected if increased channelization controlled minimum sliding speed.